



Unravelling the Electrical Conductivity of Earth and Planets

Alexander Grayver¹

Received: 11 April 2023 / Accepted: 10 October 2023 / Published online: 6 January 2024
© The Author(s) 2024

Abstract

This review presents the progress made in the last decade in the field of large-scale electromagnetic (EM) induction with natural sources, which fluctuate at periods from seconds to years and originate in oceans, ionosphere and magnetosphere. These mechanisms produce field variations that can be used to image subsurface electrical structure of Earth and planets across scales and depths from the shallow crust to the lower mantle. In the last decade, we have seen a substantial progress made in different areas related to methods, observations and 3-D numerical modelling of EM phenomena at crustal and mantle scales. Specifically, new methods for handling complex ionospheric and magnetospheric sources were proposed, accompanied by more efficient forward and inverse modelling tools that allowed us to combine several broadband sources and constrain electrical conductivity on multiple scales simultaneously. Magnetic signals due to oceanic tides were established as a new source to probe conductivity of the sub-oceanic upper mantle. Further, the launch of ESA Swarm satellites in 2013 and their successful ongoing operation have marked a new era in the field of large-scale EM induction, unlocking a set of new opportunities, but also posing new challenges. These developments were backed by new lab measurements of electrical conductivity for mantle minerals at temperatures and pressures that are getting closer to the relevant pressure and temperature conditions in the mantle, alleviating the need for inaccurate extrapolations. The latter enabled more plausible quantitative estimates of water content, melt fractions and temperature in the mantle. In parallel, crust and mantle conductivity models along with developed modelling techniques have become an integral part of geomagnetic field and geomagnetically induced currents (GICs) modelling workflows, establishing new inter-disciplinary knowledge domains.

Keywords Induction · Mantle conductivity · Geomagnetism · Magnetosphere · Ionosphere

✉ Alexander Grayver
agrayver@uni-koeln.de

¹ Institute of Geophysics and Meteorology, University of Cologne, Albertus-Magnus-Platz, 50923 Cologne, Germany

Article Highlights

- New methods for handling complex external electromagnetic sources have been developed
- Over-simplified assumptions about the external source (Z/H, also known as Geomagnetic Depth Sounding (GDS), methods) lead to biased conductivity models
- Satellite-detected magnetic fields from ocean tides represent a new induction source to study sub-oceanic upper mantle
- Untapped potential for cross-disciplinary research between Earth and Planetary sciences

1 Introduction

The field of deep electromagnetic (EM) studies has been a focus of the Division VI “Electromagnetic Induction in the Earth and Planetary Bodies” of the International Association of Geomagnetism and Aeronomy (IAGA). A number of review papers on this topic, dedicated to studies on Earth and extraterrestrial bodies, have been published in the past 50 years (Table 1). This paper continues the tradition and provides a review of the works in the field published between 2012 and 2023.

Electrical conductivity is an intrinsic physical property of minerals and rocks that EM induction methods are sensitive to. As a transport property, electrical conductivity is particularly sensitive to the presence of fluid or volatile phases in minerals, which affect both the ionic and electronic conduction. There is also a natural dependency of the conductivity on temperature. As is evident from Fig. 1, conductivity varies throughout the crust and mantle over many orders of magnitude, providing ample opportunities for studying subsurface thermo-chemical variations and helping reduce ambiguities when conductivity is analysed with other geophysical observables such as seismic velocities or density. Next to seismic properties, electrical conductivity is the *only* other physical property of rocky planets that can be imaged (in a tomographic sense) throughout the crust and the mantle. To this end, we make use of natural variations of electric and magnetic fields whose primary and induced components can be measured on the ground, at seafloor or at a spacecraft. In the latter case, only the magnetic field variations can be used, imposing certain methodological limitations compared to methods where both magnetic and electric field measurements are available. These natural variations have a broad spectrum and are induced by complex spatially distributed electric currents originating in the ionosphere, magnetosphere and oceans.

Table 1 lists previous review papers, which document the progress in the field over the past half century. However, global (large-scale) EM induction as a part of Geophysics goes back to the 19th century. Long-period EM variations observed on the ground have been used to make inferences about deep subsurface conductivity structures as early as in the work by Schuster (1889). In his work, a German-British physicist Arthur Schuster estimated the internal (inducing) and external (induced) components of the diurnal harmonics of the natural magnetic field and analysed the relation between them over the globe. This led him to conclude:

... there is strong evidence that the average conductivity is very small near the surface, but must be greater further down.

This observation was likely due to an increase in the average bulk conductivity of major mineral phases in the mantle (Fig. 1). Nowadays, we would explain such increase by a

Table 1 Review papers on large-scale electromagnetic induction studies for Earth and extraterrestrial bodies

Year of the review talk	Title	References
1972	Global electrical conductivity of the Earth	Rikitake (1973)
1972	The theory of geomagnetic induction	Price (1973)
1972	Global electromagnetic induction in the moon and planets	Dyal and Parkin (1973)
1972	Global geomagnetic sounding—methods and results	Bailey (1973)
1974	Morphology of slowly-varying geomagnetic external fields - A review	Matsushita (1975)
1974	On the inversion of global electromagnetic induction data	Anderssen (1975)
1974	Analytical solutions to global and local problems of electromagnetic induction in the Earth	Hobbs (1975)
1974	Solar-wind induction and lunar conductivity	Sonett (1975)
1978	The electrical conductivity of the moon	Vanyan (1980)
1984	Global electromagnetic induction	Roberts (1986)
1986	The global conductivity distribution	Parkinson (1988)
1998	Induction studies with satellite data	Olsen (1999a)
2010	Deep electromagnetic studies from land, sea, and space: Progress status in the past 10 years	Kuvshinov (2012)
2022	Unravelling the electrical conductivity of earth and planets—a review	This paper

positive geothermal gradient, change of mineral phases, transition from brittle to ductile or by a combination of the listed factors. His conclusions were based not only on real magnetic field observations, but also stood on solid mathematical and physical foundations. Specifically, the magnetic field observations were separated into external and internal components using the potential field representation (see Sect. 3.2) elaborated in a seminal work by Gauss (1877), whereas an effective subsurface electrical conductivity for variations at different periods was estimated using the analytical solution for a homogeneous conducting sphere (in modern taxonomy, we would call it a forward operator) derived a few years earlier by Lamb (1883), using a then still new theory of electromagnetism compounded by Maxwell (1865) and other contemporaries (Hunt 2005). It is remarkable that the work of Schuster (1889) was published long before any of the present EM induction methods had been established or practiced. It appeared even before the most fundamental aspects about the Earth’s interior, such as the presence of inner and outer cores, were discovered. A few years later, this method was developed to a stage where a global average radially varying conductivity model was invoked to better explain observations (Chapman 1919).

Despite a long and rich history, there remain vast gaps in our understanding of the Earth’s deep electrical structure. Similar to other tomographic techniques, the deeper we go into the Earth the more uncertain and low resolution our models become. By far the largest (by volume) part of the mantle remains largely a “Terra incognita” in terms of its electrical structure, leaving a big “room for improvement” for current and future generations. This review will mention some of the reasons why it is so difficult to access deeper parts of our planet with EM induction methods. Yet, this review will also show a solid progress that the

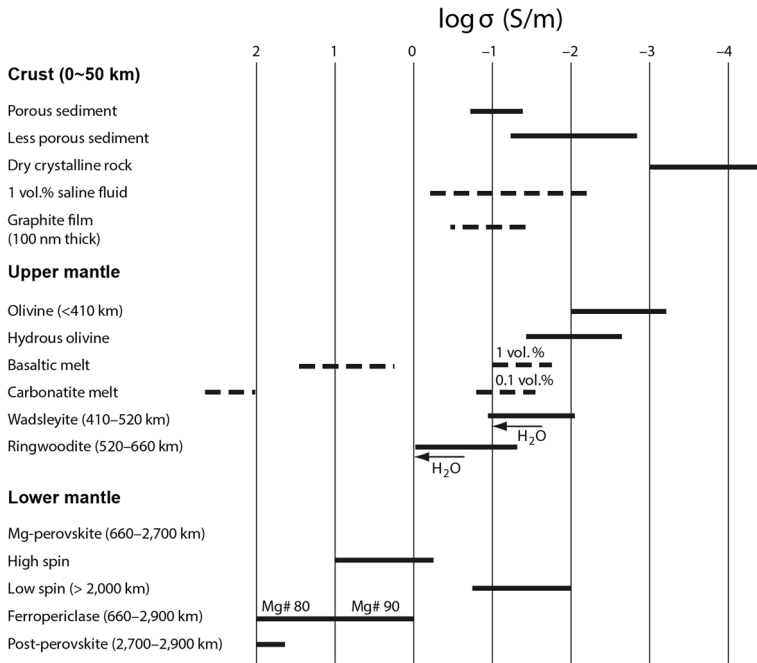


Fig. 1 Conductivity ranges for major crustal and mantle mineral phases. Adapted from Yoshino (2021)

field has experienced in the last decade, also highlighting its inter-disciplinary nature and enormous future potential.

In addition to the traditional applications of EM induction methods for studying the Earth's subsurface electrical conductivity structure, EM induction has become an integral part of research in other disciplines. For instance, large-scale EM induction modelling is essential within the Space Weather community, where it is used for modelling Geomagnetically Induced Currents (GICs) (Kelbert 2020). Another example is the use of global conductivity models to calculate the mantle induction effect while reconstructing the fast core field dynamics or external current systems from ground and satellite magnetic field observations (e.g. Chulliat et al. 2016; Sabaka et al. 2018; Finlay et al. 2020).

Although IAGA Division VI identifies induction in other planets as one of the research topics, the main focus of the division has always been on Earth. Nevertheless, Table 1 shows that the extraterrestrial research was well represented within the IAGA Division during and some time after the Apollo era, but the number of interactions between Earth and planetary sciences has since decreased. However, there has been a remarkable growth of interest in EM induction methods in planetary sciences in the last couple of decades, sustained by new observations of time-varying magnetic fields around other planets and moons, or driven by theoretical works on electromagnetic star–planet interactions. Therefore, I decided to briefly document the progress in this field in Sect. 5. I believe that there is a large potential for inter-disciplinary exchange, and trying to build more bridges with planetary sciences will facilitate the exchange of new ideas and energy, and eventually help sustain the growth of the otherwise small field.

Given the broad scope of EM induction studies in Geophysics and adjacent disciplines, it is inevitable that this review paper can cover only a part of the entire spectrum of works which invoke phenomenon of the EM induction in planets. Therefore, I shall frame the scope of this review as following:

- I will cover progress in the field from approximately 2012 to the mid 2023 unless the context requires us to refer to earlier works. Previous reviews listed in Table 1 contain a thorough coverage of earlier works.
- I will concentrate on studies which target spatial scales $\gtrsim 10^3$ km. For more regional and local studies, the reader is referred to specialized reviews.
- Topics related to Space Weather and GICs will not be covered. Please refer to a recent review by Kelbert (2020) on this topic.
- Motionally induced EM signals will be covered in the context of the subsurface conductivity imaging. For other aspects, refer to another recent review by Minami (2017).
- Implications of conductivity variations on thermo-chemical structure and advanced interpretation techniques are not covered in detail. (See recent papers by, e.g., Yoshino and Katsura 2013; Selway 2014; Pommier 2014; Khan 2016; Özyayın and Selway 2020, for more details.)
- A selection of recent studies pertaining to EM induction in other planets and extraterrestrial bodies will be covered in a dedicated Sect. 5.

2 Data and Observations

Natural variations of electric and magnetic fields are recorded on the ground, at the ocean bottom or measured in space. Table 2 lists major sources of data used in EM induction studies. Traditionally, Geomagnetic Depth Sounding (GDS) used geomagnetic observatory data to derive either local or global average transfer functions for large-scale ionospheric and magnetospheric sources. However, one quickly reaches a limit imposed by this data set. As is evident from Fig. 2, despite some observatories were around for more than a century, the overall global coverage has always been uneven and very sparse in the southern hemisphere and over the oceans. Adding to this many large time gaps in data imposes significant constraints on what this data set allows one to do in terms of the subsurface conductivity imaging. Due to substantial multi-institutional and international efforts within the Intermagnet consortium (Love and Chulliat 2013), the number of simultaneously operating observatories reached from 120 to 140, although the potential of growing this network further is limited. In fact, a decrease in the number of operating worldwide observations has been recently observed. Yet, permanent observatories is the observational backbone of geomagnetic community and continue to find new usages in geophysics (Thomson and Flower 2021). A decade ago, British Geological Survey (BGS) initiated and since then maintains a real-time pre-processed and quality-controlled database of permanent present and legacy geomagnetic data with cadence ranging from 1 sec to 1 day (Macmillan and Olsen 2013). This development, primarily aimed at supporting ESA Swarm science activities, became a particularly useful development for the EM community, removing a huge burden of processing and calibrating observatory data. As a result, many recent EM induction studies that used geomagnetic observatories relied on this database.

Limited coverage of the geomagnetic observatory network can be partially mitigated by including other sources of data, in particular magnetic variometer instruments. First, some regional to continental-scale arrays, such as SuperMAG (Gjerloev 2012), IMAGE (Tanskanen 2009), and AWAGS (Chamalaun and Barton 1990), provide recordings of sufficient length and quality to enable mantle sounding. These networks have been focused on supporting the external field studies, but, as we shall see later, were proven useful for the subsurface conductivity imaging (see Sect. 4.3).

Table 2 Major sources of data and their main characteristics

Data type	Advantages	Limitations	Data sources ¹
Temporary stations (arrays)	Improved local resolution	short time series	USArray, AusLAMP, SinoProbe, AWAGS, IMAGE, SuperMAG
Geomagnetic observatories	Long high-quality time series	sparse uneven coverage	INTERMAGNET, National Geological Surveys
Dedicated space science missions	High quality, uniform spatial coverage	space-time aliasing, limited local-time coverage	CHAMP, Swarm, Ørsted, MSS-1 (launched 2023), NanoMagSat (planned)
Satellite platform magnetometers	Unprecedented spatiotemporal coverage	reduced accuracy, ad-hoc calibrating procedures	CryoSat-2, GRACE-FO, GOCE, DMSP, Iridium

¹This list is not exhaustive

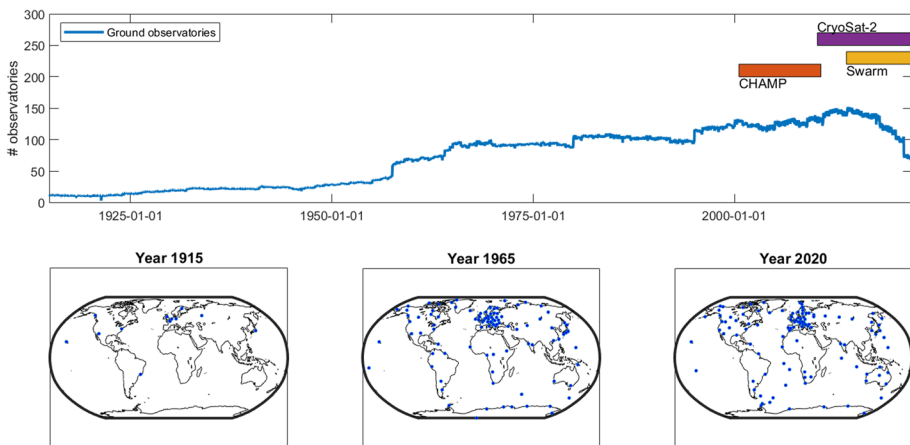


Fig. 2 Top: number of available ground magnetic observatories versus time as well as the time span of some modern satellite missions (coloured rectangles). Bottom: Distribution of ground magnetic observatories with definitive data for three selected years in the past century as per (Macmillan and Olsen 2013) database. Note the lack of ground-based observations in southern hemisphere and over the oceans throughout the time. A quick decrease towards 2020 is due to a lag in the publication of definitive data

A major highlight of the past decade has been the progress in the completion of national magnetotelluric (MT) arrays (Fig. 3), most notably USArray (different parts of the array were acquired within a number of independently funded projects and have different names, but for the sake of clarity we will call the combined dataset USArray) (Schultz 2010; Schultz et al. 2018, 2020, 2023), AusLAMP (Thiel et al. 2020; Duan et al. 2020, among others) and SinoProbe (e.g. Dong et al. 2013). Noteworthy, data from USArray and AusLAMP are open to public and present unique data sets that already led to high-quality research output in subsurface imaging (see Sect. 4.1) and space weather studies (Kelbert 2020). Although recording times at individual locations do not typically exceed one month, this is sufficient to derive MT transfer functions up to periods of 5–7 h, which allows one to image electrical conductivity through the lithosphere and parts of asthenosphere. Some instruments deployed at the seafloor were also used for large-scale EM studies during the past decade (e.g. Matsuno et al. 2017), although the spatial extent and density of these

surveys are limited by logistical and cost reasons. Similar efforts have been undertaken by several other countries, for instance, UK (Huebert et al. 2022) and Portugal (Baltazar-Soares et al. 2023). Compilation of existing and legacy data sets can sometimes result in a quasi-regular national-wide network, although at the cost of heterogeneous quality of data, unknown survey characteristics and sometimes missing raw time series. A good example is a map of MT data in the Northern Europe (Fig. 3) compiled by Prof. M. Smirnov showing dozens of MT arrays (e.g. Korja et al. 2002; Cherevatova et al. 2015; Autio and Smirnov 2020, among others). Some of these and further regional and local array data can also be found on national and international data archiving portals established in the last decade.¹²

The primary goals of collecting these array MT data are twofold: (i) more accurate evaluations of Geomagnetically Induced Currents (GICs) and (ii) improved knowledge of subsurface geology and tectonics. This represents a clear example of how progress in one discipline immediately leads to advances in the other and vice versa. It is likely that more country-wide MT arrays will be initiated in the next decade.

So far, we discussed only observations performed on the ground or at the seafloor. Since the beginning of the twenty-first century, we have nearly continuous satellite geomagnetic observations from dedicated missions (Fig. 2). Previous reviews have already covered earlier attempts in using satellite data for EM induction studies (Olsen 1999a; Kuvshinov 2012). A major milestone of the past decade was the launch of three ESA Swarm satellites in November 2013 (Olsen et al. 2013), which are still in operation (as of September 2023). Swarm satellites are flying on low Earth polar orbits, whereby the lower pair (≈ 430 km altitude as of May 2022), called Swarm A and C, are flying with a very small longitudinal separation (few degrees) and an upper (≈ 500 km as of May 2022) Swarm B spacecraft has a precessing orbit with a dynamic local-time separation relative to the lower pair. It takes around three months for satellites to cover all local times. In recent years, Swarm data was used to produce a series of global conductivity models (see Sects. 4.4 and 4.2). However, outstanding accuracy of satellite data and nearly uniform global coverage come with a set of methodological challenges. Since satellites move very quickly (≈ 90 min per orbit), there always exists a trade-off between how well space and time variations in magnetic field can be simultaneously resolved. Since there are many natural sources that vary quickly in space and time, this may result in space-time aliasing. Furthermore, satellites at polar orbits have a limited local-time (LT) coverage. In practice, a single Swarm satellite covers only two local times per each orbit, whereas most external induction sources are local-time phenomena (Finlay et al. 2017; Ganushkina et al. 2018) and require a dense LT sampling for reliable separation and reconstruction. Additionally, low Earth orbit (LEO) satellites fly above prominent ionospheric dynamo regions and through the regions with field-aligned currents (FACs), making it difficult to separate ionospheric and mantle contributions, although new methods described in Sect. 3 will help in mitigating these challenges.

We also briefly note that some further dedicated missions are planned, including for instance a European NanoMagSat (Hulot et al. 2021) and Chinese Macau Science Satellite (MSS) constellation missions. These constellations will deploy satellites on low-inclination and elliptic orbits in addition to satellites on polar orbits. This will result in a much faster and denser local-time coverage, thus enabling a more reliable inducing source field estimation. Finally, conceptually new ideas of remote “mapping” of magnetic fields using the Zeeman effect are proposed within the NASA’s

¹ <https://ds.iris.edu/spud/emtf>.

² <https://www.ics-c.epos-eu.org/>.

Fig. 3 Examples of national-wide MT arrays. Top panels show the state of the AusLAMP survey (image by *Geoscience Australia*) and USArray sites extracted from the IRIS database (as of August 2023) (Kelbert et al. 2019b). Middle panels shows nation-wide MT arrays from Portugal (modified after (Baltazar-Soares et al. 2023)) and UK (images courtesy of Dr. J. Hübert, see Huebert et al. (2022)). Bottom most figure is a compilation of national and international MT arrays collected over last decades in Northern Europe (image courtesy of Prof. M. Smirnov), e.g. (Korja et al. 2002; Cherevatova et al. 2015; Autio and Smirnov 2020)

Electrojet Zeeman Imaging Explorer (EZIE), scheduled for a launch in 2024 (Laundal et al. 2021). To which extent this concept can directly facilitate EM induction studies remains to be understood, but a much better understanding of ionospheric currents enabled by this mission will certainly have an indirect influence on the mantle induction studies through better external source models, provided there is enough will in the community to borrow and adapt knowledge from adjacent fields.

Next to dedicated science missions, it is known that many (hundreds to thousands) satellites carry the so-called platform magnetometers. These instruments' primary use is an auxiliary attitude control, yet the quality of some instruments and design of spacecraft platforms allows for their scientific usage. There has been a substantial effort in the community recently to calibrate data from platform magnetometers and make them available for community (Olsen et al. 2020; Stolle et al. 2021; Styp-Rekowski et al. 2022; Alken et al. 2020; Anderson et al. 2021). Table 2 lists some of the missions with available calibrated data from platform magnetometers. Notably, data from the CryoSat-2 mission was already used in global EM induction studies in conjunction with the Swarm and ground observatories (Velínský and Knopp 2021; Kuvshinov et al. 2021). Many problems pertaining to the calibration and processing of these data remain, but it is already clear that platform magnetometers can add value, especially by improving the local-time coverage (Fig. 4) or filling in time gaps where dedicated satellites were not in operation, thus playing an important role in constraining the fast-varying external source currents (Olsen 2007; Finlay et al. 2017).

3 Methods

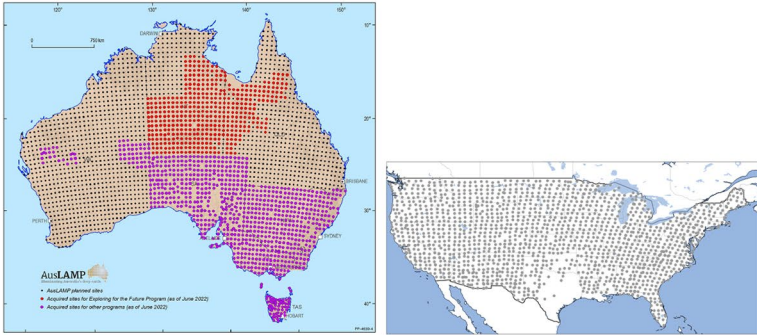
The goal of this section is to give a succinct introduction to the methods and governing equations that are used in large-scale EM induction studies. More detailed derivations may be found in the referenced papers and previous EM reviews (Table 1).

3.1 Governing Equations

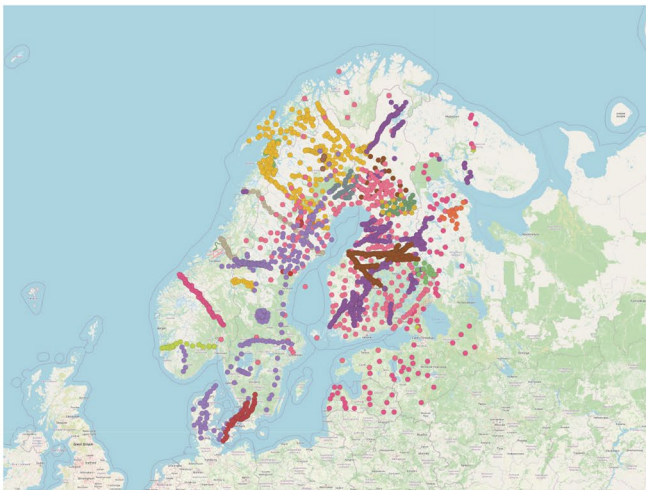
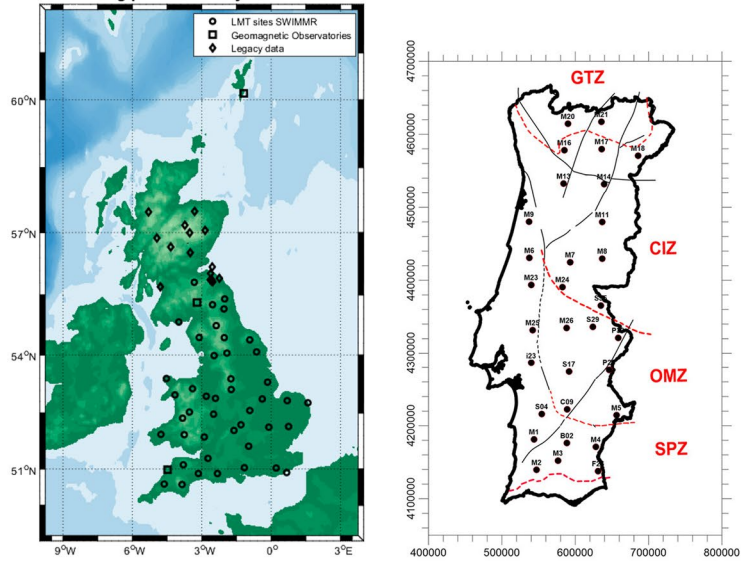
Natural electromagnetic fields used for large-scale EM induction studies are governed by a system of partial differential equations (PDEs) known as Maxwell's equations in matter:

$$\nabla \times \vec{H} = \sigma \vec{E} + \frac{\partial \vec{D}}{\partial t} + \vec{j}^{\text{ext}}, \quad (1)$$

$$\nabla \times \vec{E} = - \frac{\partial \vec{B}}{\partial t}, \quad (2)$$



Long-period MT array in the UK



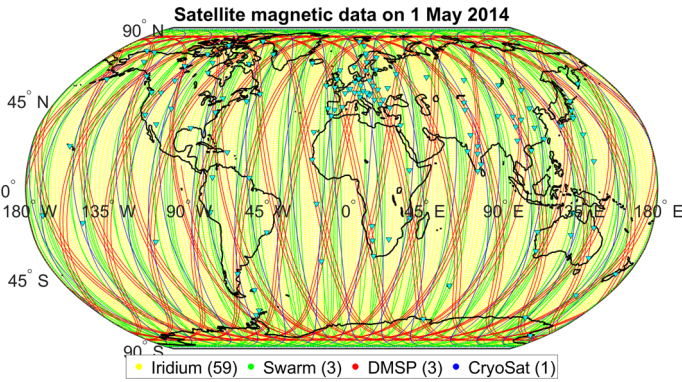


Fig. 4 Single day orbits of the dedicated geomagnetic ESA Swarm satellites and a selection of satellites carrying platform magnetometers. Separate orbits of the Iridium constellation (yellow) are difficult to distinguish due to a very high density of measurements. Triangles depict geomagnetic observatories

$$\nabla \cdot \vec{B} = 0, \tag{3}$$

$$\nabla \cdot \vec{D} = \rho_f, \tag{4}$$

where \vec{H} is magnetic field intensity [A/m], \vec{E} electric field intensity [V/m], \vec{B} magnetic flux density [T] or [Vs/m²], \vec{D} electric flux density [As/m], and ρ_f electric charge density [C/m³]. We assume a linear medium without additional polarization and magnetization, resulting in the following constitutive equations

$$\vec{H} = \frac{1}{\mu} \vec{B}, \tag{5}$$

$$\vec{D} = \epsilon \vec{E}, \tag{6}$$

where μ is magnetic permeability [Vs/Am] and ϵ is electric permittivity [As/Vm]. Note that corresponding vacuum constants for the permeability and permittivity are assumed throughout the volume, that is $\mu \equiv \mu_0, \epsilon \equiv \epsilon_0$. Our modelling domain is a sphere (or a spherical shell) with a heterogeneous distribution of the electrical conductivity $\sigma \equiv \sigma(\vec{r})$ [S/m]. Here, $\vec{r} = (r, \theta, \phi)$ denotes a position vector in the spherical coordinate system with the origin at the sphere’s centre and r, θ and ϕ being distance from the planet’s centre, polar angle (co-latitude), and azimuthal angle (longitude), respectively. For the boundary conditions, we assume that fields decay to zero sufficiently fast as $r \rightarrow \infty$ and satisfy the Helmholtz theorem (Griffiths 2017).

The right-hand side of Eq. (1) represents the total current density [A/m²] given by the sum of the conduction current (also called free current), displacement current and the extraneous (impressed) electric current density. The extraneous current density term is not part of the original Maxwell’s equations. Instead, it is added for the practical convenience, in order to represent our sources in some form that is amenable to subsequent data analysis and modelling (Table 3).

For a relevant range of material properties, space dimensions and periods of variations, the displacement current term can be neglected from the complete Maxwell’s equations,

resulting in the so-called quasi-static *approximation*. Under the quasi-static approximation, the set of equations is sometimes referred to as pre-Maxwell’s equations (Hunt 2005) and read

$$\frac{1}{\mu} \nabla \times \vec{B} = \sigma \vec{E} + \vec{j}^{\text{ext}}, \tag{7}$$

$$\nabla \times \vec{E} = - \frac{\partial \vec{B}}{\partial t}. \tag{8}$$

Quasi-static (sometimes also termed quasi-stationary) approximation incurs a number of fundamental consequences. For instance, it partially invalidates the Coulomb’s law, implies an instantaneous propagation (because of $c \rightarrow \infty$, where c is the speed of light) and makes it hard to understand how our inducing source EM fields reach the ground despite assuming electrically insulating (i.e. $\sigma \rightarrow 0$) layers of the atmosphere. We shall not argue that the quasi-static approximation is justified in practice and provides means for explaining our observations in the relevant physical regime, yet internal inconsistencies therein may generate some confusion when physical interpretation of electrodynamic phenomena is sought. It is notable that already first IAGA EM review papers contain discussion about *non sequiturs* of the quasi-static approximation (Price 1973). An in-depth analysis of physical consequences and implications of the quasi-static approximation was presented in insightful works by Everett and Chave (2019), Berdichevsky and Dmitriev (2002) focusing on geophysical context or from a more general physics standpoint by Larsson (2007).

For the purposes of this review, it will be necessary to carry out derivations and perform data modelling in the frequency domain. Adopting the Fourier convention

$$f(t) = \frac{1}{2\pi} \int_{-\infty}^{\infty} F(\omega) e^{-i\omega t} d\omega \tag{9}$$

allows us to rewrite Ampere’s and Faraday’s laws (7-8) in the frequency domain as

$$\frac{1}{\mu} \nabla \times \vec{B} = \sigma \vec{E} + \vec{j}^{\text{ext}}, \tag{10}$$

$$\nabla \times \vec{E} = i\omega \vec{B}, \tag{11}$$

where ω is the angular frequency. In what follows and unless otherwise stated, we will work in frequency domain, implying dependency on ω for electromagnetic fields and derived variables.

3.1.1 Current Density Representation

Without loss of generality, we can represent the extraneous current density, $\vec{j}^{\text{ext}}(\vec{r}, \omega)$, as a linear combination of spatial modes $\vec{j}_i(\vec{r})$ and frequency-dependent coefficients c_i as

$$\vec{j}^{\text{ext}}(\vec{r}, \omega) = \sum_i \vec{j}_i(\vec{r}) c_i(\omega), \tag{12}$$

where spatial modes $\vec{j}_i(\vec{r})$ can be given by electric dipoles, current loops or continuous global functions (see Sect. 3.5 for some specific examples).

By virtue of the linearity of Eqs. (10)–(11) with respect to the $\vec{j}^{\text{ext}}(\vec{r}, \omega)$ term, we can expand the total (that is, inducing plus induced parts) electromagnetic field as a linear combination of individual fields \vec{B}_i, \vec{E}_i ,

$$\vec{B}(\vec{r}, \omega; \sigma) = \sum_i \vec{B}_i(\vec{r}, \omega; \sigma) c_i(\omega), \tag{13}$$

$$\vec{E}(\vec{r}, \omega; \sigma) = \sum_i \vec{E}_i(\vec{r}, \omega; \sigma) c_i(\omega), \tag{14}$$

where fields $\vec{B}_i(\vec{r}, \omega; \sigma)$ and $\vec{E}_i(\vec{r}, \omega; \sigma)$ are fields induced by individual spatial modes with unit coefficients. Hence, they are solutions of the equations

$$\frac{1}{\mu_0} \nabla \times \vec{B}_i = \sigma \vec{E}_i + \vec{j}_i, \tag{15}$$

$$\nabla \times \vec{E}_i = i\omega \vec{B}_i, \tag{16}$$

and represent EM transfer functions of a medium (Püthe et al. 2015b; Guzavina et al. 2019; Grayver et al. 2021). Therefore, a transfer function of a conductive body (planet or moon) at a position \vec{r} depends on the subsurface conductivity distribution and frequency of excitation as well as on the spatial geometry of the current density expressed through the \vec{j}_i term.

3.1.2 Thin-Sheet Equivalent Current

The true geometry and distribution of the current density given by the term \vec{j}^{ext} are very complicated in reality and generally not known. However, assuming that electric currents flow within spherical shell embedded in an insulator above the ground, allows us to represent any current density distribution within the shell using a thin sheet current (Schmucker 1985; Sabaka et al. 2010) characterized by a stream function

$$\vec{j}^{\text{ext}}(\vec{r}, \omega) = -\delta(r - b)\hat{e}_r \times \nabla_H \Psi(\theta, \phi, \omega), \tag{17}$$

where a is the mean radius of the Earth, $b = a + h$, with $h > 0$ being the altitude of the current sheet;

$$\nabla_H f = \frac{1}{r} \frac{\partial f}{\partial \theta} \hat{e}_\theta + \frac{1}{r \sin \theta} \frac{\partial f}{\partial \phi} \hat{e}_\phi \tag{18}$$

is the angular part of the gradient operator and $\hat{e}_r, \hat{e}_\theta$ and \hat{e}_ϕ are the unit vectors of the spherical coordinate system. Consequently, we can expand the stream function using spatial modes and scalar coefficients, thus

$$\Psi(\theta, \phi, \omega) = \sum_i \Psi_i(\theta, \phi) c_i(\omega). \tag{19}$$

Using Eqs. (12) and (19), we can rewrite Eq. (17) as

$$\vec{j}^{\text{ext}}(\vec{r}, \omega) = -\delta(r - b) \sum_i [\hat{e}_r \times \nabla_H \Psi_i(\theta, \phi)] c_i(\omega). \tag{20}$$

3.2 Potential Field Representation

Above the ground and in the source-free region, Eq. (10) reduces to $\nabla \times \vec{B} = 0$. Therefore, \vec{B} is a potential field and can be written as

$$\vec{B} = -\nabla V. \tag{21}$$

By virtue of Gauss’ law of magnetism, $\nabla \cdot \vec{B} = 0$. Thus, a scalar potential V satisfies the Laplace’s equation,

$$\nabla^2 V = 0. \tag{22}$$

Solution of the Eq. (22) can be written as a sum of the external and internal potentials, that is $V = V^{\text{ext}} + V^{\text{int}}$. In the context of EM induction problems, external and internal components represent “inducing” and “induced” parts of the magnetic field, respectively. Thus, the internal part of the potential also depends on the subsurface conductivity. Adding the dependency on the location, frequency (respectively time), and subsurface conductivity, the total potential can be written as

$$\begin{aligned} V(\vec{r}, \omega) &= V^{\text{ext}}(\vec{r}, \omega) + V^{\text{int}}(\vec{r}, \omega; \sigma) \\ &= a \sum_{n,m} \varepsilon_n^m(\omega) \left(\frac{r}{a}\right)^n S_n^m(\theta, \phi) + a \sum_{k,l} i_k^l(\omega; \sigma) \left(\frac{a}{r}\right)^{(k+1)} S_k^l(\theta, \phi), \end{aligned} \tag{23}$$

where

$$S_n^m(\theta, \phi) = P_n^{|m|}(\cos \theta) \exp(im\phi) \tag{24}$$

is a spherical harmonic (SH) function of degree n and order m with $P_n^{|m|}$ being Schmidt semi-normalized associated Legendre polynomials, and $\varepsilon_n^m(\omega)$ and $i_k^l(\omega; \sigma)$ are the SH expansion coefficients of the external (inducing) and internal (induced) origins, respectively. Hereinafter, we will adopt the following convention

$$\sum_{n,m} = \sum_{n=1}^{\infty} \sum_{m=-n}^n. \tag{25}$$

Equations (21) and (23) allow us to write the (poloidal) magnetic field above the ground as

$$\vec{B}(\vec{r}, \omega) = \vec{B}(\vec{r}, \omega)^{\text{ext}} + \vec{B}(\vec{r}, \omega; \sigma)^{\text{int}} \tag{26}$$

or in the component form

$$\begin{aligned}
 B_r = & - \sum_{n,m} n \varepsilon_n^m(\omega) \left(\frac{r}{a}\right)^{n-1} S_n^m(\theta, \phi) \\
 & + \sum_{k,l} (k+1) l_k^l(\omega; \sigma) \left(\frac{a}{r}\right)^{k+2} S_k^l(\theta, \phi),
 \end{aligned}
 \tag{27}$$

$$\begin{aligned}
 \vec{B}_r = & - \sum_{n,m} \varepsilon_n^m(\omega) \left(\frac{r}{a}\right)^{n-1} \nabla_{\perp} S_n^m(\theta, \phi) \\
 & - \sum_{k,l} l_k^l(\omega; \sigma) \left(\frac{a}{r}\right)^{k+2} \nabla_{\perp} S_k^l(\theta, \phi),
 \end{aligned}
 \tag{28}$$

where $\nabla_{\perp} = r \nabla_H$. Now, SH functions can be used as a basis in Eq. (19). For a source of the external origin, the stream function can be written as (Schmucker 1985)

$$\Psi^e(\theta, \phi, \omega) = -\frac{a}{\mu_0} \sum_{n,m} \frac{2n+1}{n+1} \left(\frac{b}{a}\right)^n \varepsilon_n^m(\omega) S_n^m(\theta, \phi),
 \tag{29}$$

which in turn allows us to rewrite Eq. (20) as

$$\vec{j}^{\text{ext}}(\vec{r}, \omega) = \sum_{n,m} \vec{j}_n^m(\vec{r}) \varepsilon_n^m(\omega),
 \tag{30}$$

with

$$\vec{j}_n^m(\theta, \phi) = \frac{\delta(r-b)}{\mu_0} \frac{2n+1}{n+1} \left(\frac{b}{a}\right)^{n-1} \hat{e}_r \times \nabla_{\perp} S_n^m(\theta, \phi).
 \tag{31}$$

It can be shown (Schmucker 1985; Sabaka et al. 2010; Kuvshinov and Semenov 2012) that the electric currents in Eqs. (30)–(31) flowing within a shell at $r = b$ produce the external magnetic field B^{ext} in region $r \in [a, b)$ exactly.

Both ionospheric and magnetospheric sources are of external origin for ground measurements and Eqs. (29)–(31) can be used to represent the equivalent current system and reproduce the external field in Eqs. (26)–(28). However, at a low Earth orbit (LEO) satellite, for instance at ESA Swarm satellites flying at $\approx 400 - 550$ km altitude, both primary fields generated in the ionospheric E-region and fields induced in the subsurface are of internal origin, whereas fields generated by major magnetospheric source currents remain to be external. In addition, some in situ currents can generate toroidal magnetic field (Lühr et al. 2002; Olsen 1997) and invalidate the potential field assumption (i.e. $\nabla \times \vec{B} \neq 0$). These complications are among the main reasons why interpretation of satellite data is more nuanced and complicated compared to ground data. As a result, Eqs. (29)–(31) can still be used to model magnetospheric fields with observations from LEO satellites, but are no longer valid for representing E-region ionospheric fields. Nevertheless, a physically consistent description of the ionospheric fields at LEO satellites can still be achieved under certain assumptions, as elaborated by Sabaka et al. (2002, 2010), Chulliat et al. (2016). In these studies, a prior subsurface conductivity model is used, which allows one to co-model the field induced in the mantle and then estimate the corresponding ionospheric source current.

Note that the potential field representation such as the one in Eq. (22) is not valid for a time-varying electric field. Furthermore, inside the conductive Earth, $\nabla \times \vec{B} \neq 0$ and Eq.

(21) no longer holds even for the magnetic field. Instead, we can resort to Eqs. (13)–(14) and express total electric and magnetic fields at a position \vec{r} inside the Earth as

$$\vec{B}(\vec{r}, \omega; \sigma) = \sum_{n,m} \vec{B}_n^m(\vec{r}, \omega; \sigma) \epsilon_n^m(\omega), \tag{32}$$

$$\vec{E}(\vec{r}, \omega; \sigma) = \sum_{n,m} \vec{E}_n^m(\vec{r}, \omega; \sigma) \epsilon_n^m(\omega). \tag{33}$$

For a radial conductivity structure, $\sigma(\vec{r}) \equiv \sigma(r)$, both electric and magnetic fields inside a conducting body can be expressed by means of a spectral impedance Z_n . At the surface, analytic expressions for the field components can be written as (Kuvshinov and Semenov 2012)

$$\vec{E}_\tau(\vec{r}_a, \omega; \sigma) = -\frac{1}{\mu_0} \sum_{n,m} \frac{2n+1}{n+1} \epsilon_n^m(\omega) \frac{i\omega\mu_0 a Z_n}{i\omega\mu_0 a - nZ_n} \hat{e}_r \times \nabla_\perp S_n^m(\theta, \phi), \tag{34}$$

$$B_r(\vec{r}_a, \omega; \sigma) = \sum_{n,m} (2n+1)n \epsilon_n^m(\omega) \frac{Z_n}{i\omega\mu_0 a - nZ_n} S_n^m(\theta, \phi), \tag{35}$$

$$\vec{B}_\tau(\vec{r}_a, \omega; \sigma) = -\sum_{n,m} \frac{2n+1}{n+1} \epsilon_n^m(\omega) \frac{i\omega\mu_0 a}{i\omega\mu_0 a - nZ_n} \nabla_\perp S_n^m(\theta, \phi). \tag{36}$$

Here, $Z_n \equiv Z_n(a, \omega; \sigma)$ is the spectral impedance of a spherical conductor (e.g. Srivastava 1966) and $\vec{r}_a = (r \rightarrow a-, \theta, \phi)$ denotes a position at the Earth’s surface where r approaches the surface from below.

For the sake of brevity, the dependency on location and frequency was sometimes omitted above, but can be easily inferred from the context.

3.3 Global Response Functions

Unlike in the MT method (that is, under the plane-wave approximation), there is no universal transfer function like the impedance tensor that fully describes Earth’s induction response to a time-varying external current at periods longer than several hours, at least not in an equivalent compact form. In this and the next sections, I will give a short summary of the conventionally used response functions for mantle-scale studies. Whenever possible, I will try to establish a link between response functions and the governing equations laid down in the previous section.

In the previous section, the dependency of the induced (internal) field on the conductivity was explicitly stated. Additionally, the connection between the inducing and induced magnetic fields follows from Eqs. (27)–(32). Using the potential representation of the magnetic field above the ground (Eqs. 27–28) and assuming a 1-D subsurface conductivity structure ($\sigma(\vec{r}) \equiv \sigma(r)$), the relation can be formally written as

$$i_n^m(\omega; \sigma) = Q_n(\omega; \sigma) \epsilon_n^m(\omega), \tag{37}$$

where Q_n is a global induction response (transfer) function (Bailey 1973; Schmucker 1985). Note that for a 1-D Earth, each external mode induces only one internal mode and Q_n is

independent of order m under this assumption. Using Eq. (37), we can introduce another global response function, C -response, as (see Table II in Olsen (1999a))

$$C_n(r) = \frac{r}{n+1} \frac{\left(\frac{r}{a}\right)^{2n+1} - \frac{n+1}{n} Q_n}{\left(\frac{r}{a}\right)^{2n+1} + Q_n} \quad (38)$$

where $r \geq a$. Hence, unlike the Q -response, C -response depends on the radius. Further, C -response can also be defined through the spectral impedance as

$$Z_n = -i\omega\mu_0 C_n, \quad (39)$$

where dependency on r , ω and σ was omitted for brevity. Mathematical and physical properties of the C -response function have been investigated in the seminal work by Weidelt (1972). In practice, Q_n and C_n can be estimated at selected frequencies using time series of ground or satellite magnetic field observations or a combination thereof.

Resorting to a general case with a 3-D subsurface conductivity distribution invalidates equations above. In this case, each external mode e_n^m induces infinitely many coupled internal modes (Olsen 1999a). The relation between inducing and induced coefficients is then described by a set of transfer functions called the Q -matrix

$$t_k^l(\omega; \sigma) = \sum_{n,m} Q_{kn}^{lm}(\omega; \sigma) e_n^m(\omega). \quad (40)$$

Formally, the Q -matrix represents a complete induction response of the 3-D Earth to an arbitrary inducing current as defined in Eq. (30). Importantly, Q -matrix is fully compatible with the satellite data since it does not explicitly depend on the location. However, since SH functions have a global footprint, high truncation degrees k are required in order to describe conductivity variations on scales below 10^4 km (compare λ versus SH degree in Fig. 6). This implies that a large number of terms of the Q -matrix need to be estimated from typically sparse and noisy data. More information on the calculation and properties of the Q -matrix can be found in Püthe and Kuvshinov (2014).

3.4 Local Response Functions

Previous section described commonly used global response (transfer) functions (TF). The advantage of a global TF is that the effects of space and time can be conveniently separated, enabling easier workflows for satellite data assimilation since satellites are constantly moving. However, most ground or ocean-bottom EM observations have a fixed location in the mantle frame, therefore it is natural to resort to transfer functions that can be linked to a location at the surface or seafloor. In fact, local TFs were elaborated long before the satellite era came. As a result, none of the local responses discussed below can be easily reconciled with satellite data workflows.

3.4.1 Plane-Wave Sources

Magnetotellurics (MT) is the most widely used natural EM induction method. As a method, MT rests on the plane-wave source assumption, which, if valid, allows one to fully factor out

the source term from governing equations and derive a set of complete transfer functions that can be used to image the 3-D subsurface conductivity distribution.

Assume a flat Earth extending infinitely in horizontal directions with a corresponding local Cartesian coordinate system with x, y, z pointing to the North, East, and Down respectively (with $z = 0$ at the surface). In this reference frame, a vertically incident plane wave can be represented. Assume \vec{E}, \vec{H} are electric and magnetic fields due to a current density

$$\vec{j}^{\text{ext}} \equiv \mu_0^{-1} \hat{z} \times \vec{B}_0 \delta(z - h), \tag{41}$$

where \vec{B}_0 is a quasi-uniform, horizontal, external source magnetic field at the altitude h , \hat{z} is a unit axis vector (for brevity, the conversion from spherical to local reference frames is implied). These fields must obey equations (10-11). Then, the frequency-dependent MT impedance tensor, \mathbf{Z} , at the surface relates horizontal electric and magnetic field components as

$$\begin{pmatrix} E_x \\ E_y \end{pmatrix} = \begin{pmatrix} Z_{xx} & Z_{xy} \\ Z_{yx} & Z_{yy} \end{pmatrix} \begin{pmatrix} H_x \\ H_y \end{pmatrix}, \tag{42}$$

Note that all quantities in Eq. (42) are functions of frequency, position and subsurface conductivity. Impedance tensor, \mathbf{Z} , is a transfer function that fully describes an EM induction response of a flat conductive medium due to an infinite plane-wave source. Naturally, these assumptions are justified only up to a certain spatial scale and period of variation. Formal conditions for which the impedance remains a valid transfer function are rather technical and were elaborated by Berdichevsky and Dmitriev (2002). For Eq. (42) to be a valid TF, a necessary (although not sufficient) condition is that the source field must vary slowly over a distance of a few skin depths, δ_s , that is

$$\lambda(\omega) \gg \sqrt{\frac{2}{\omega \mu_0 \sigma_h}}, \tag{43}$$

where $\lambda(\omega)$ is the spatial scale of the source field for a given angular frequency and a homogeneous Earth conductivity σ_h . Thanks to this, we can avoid the flat-Earth assumption and resort to a different class of source functions, which fulfil Eq. (43) and allow us to calculate valid MT transfer functions on a sphere (e.g. Grayver et al. 2019; Kruglyakov and Kuvshinov 2022).

3.4.2 Spherical Harmonic Sources

Assuming that the external inducing field is described by a *single* spherical harmonic S_n^m, C_n -response can also be defined using local electric and magnetic fields. Employing Eq. (39) together with Eqs. (34)–(36) yields

$$C_n(a, \theta, \phi; \sigma) = \frac{1}{\sin \theta} \frac{a}{n(n+1)} \frac{\partial_\phi S_n^m(\phi, \theta)}{S_n^m(\phi, \theta)} \frac{B_r(a, \theta, \phi, \omega; \sigma)}{B_\phi(a, \theta, \phi, \omega; \sigma)} \tag{44}$$

$$= \frac{a}{n(n+1)} \frac{\partial_\theta S_n^m(\phi, \theta)}{S_n^m(\phi, \theta)} \frac{B_r(a, \theta, \phi, \omega; \sigma)}{B_\theta(a, \theta, \phi, \omega; \sigma)}. \tag{45}$$

If the electric field is available (this is rarely the case in practice), we can also write

$$C_n(a, \theta, \phi; \sigma) = -\frac{1}{i\omega\mu_0} \frac{E_\phi(a, \theta, \phi, \omega; \sigma)}{B_\theta(a, \theta, \phi, \omega; \sigma)} \quad (46)$$

$$= \frac{1}{i\omega\mu_0} \frac{E_\theta(a, \theta, \phi, \omega; \sigma)}{B_\phi(a, \theta, \phi, \omega; \sigma)}. \quad (47)$$

Note that for zonal harmonics, S_n^0 , Eqs. (44) and (47) are not valid due to zero denominator.

Finally, when the geometry of the inducing field is described by the first *zonal* harmonic S_1^0 , we arrive at the well-known expression

$$C_1 = -\frac{a}{2} \tan \theta \frac{B_r}{B_\theta}, \quad (48)$$

which forms the core of the *Z/H* method first elaborated by Banks (1969).

It should be stressed again that Eqs. (44)–(48) are valid *only if* the external field variations in corresponding electric and magnetic field components are produced by an external electric current source that is given by a single SH function (that is, by the form given in Eq. 31). In reality, this is never the case (Ganushkina et al. 2018) and only rarely this assumption holds to a degree where source effects due to other than P_1^0 coefficients can be neglected. Although many studies have clearly demonstrated this and a significant effort has been made to overcome this limitations, many recent studies (see Sect. 4) directly apply Eq. (48) to real data without considering realistic source complexity and invert distorted C_1 responses for a 3-D subsurface conductivity distribution. The consequences of such simplistic approach is that the source effects propagate to the subsurface conductivity model in an uncontrolled way and are very likely to result in conductivity variations that are artefacts not caused by variations in subsurface composition and temperature. This point will be demonstrated in an experiment involving real data in Sect. 3.5.3.

A set of local transfer functions that would remain valid for complex non-plane-wave sources (that is, when the source cannot be represented by a single spatial mode) from daily and magnetospheric bands was presented by Schmucker (2018). This work, translated and published posthumously, documents the author's attempt to unify plane wave, GDS and the so-called horizontal spatial gradient (HSG) methods (see Kuvshinov (2012) for a detailed description of the HSG method). However, to be applicable in practice, this approach requires a locally dense network of simultaneous observations, limiting its practical application. In the last decade, new approaches that can handle complex external sources and do not suffer from limitations of the conventional methods described above were developed. These approaches will be discussed in the subsequent sections.

Finally, note that none of the local responses discussed above can be easily reconciled with satellite data since a spacecraft does not have a fixed position in the mantle frame.

3.5 Representation of External Sources

Earth has a complex and diverse natural electromagnetic environment. The quality of the subsurface conductivity models in the field of mantle-scale EM induction studies depends strongly on how well we are able to model or represent primary source currents. As is evident from Fig. 7, spectrum of natural EM variations is very broad and dense. The major part of the primary (inducing) source field originates in the ionosphere and magnetosphere, although primary EM fields are also generated within the oceans (Minami 2017). To keep

this review focused, I assume that geomagnetic variations from the Earth's core were subtracted from the data, but an interested reader will find a more complete spectrum of the total geomagnetic field including the core field component in Constable and Constable (2023). Further, we excluded part of the spectrum with natural variations induced by atmospheric phenomena in layers below the ionosphere. These phenomena mostly give rise to short period EM variations (Constable and Constable 2023) suitable for sounding sediments and shallow crustal layers, which are beyond the scope of this review paper.

In addition to strong periodic signals, such as those related to the orbital rotation, ionospheric resonances and tides, a significant part of EM time variations are due to aperiodic transient events, to a large extent driven and/or modulated by dynamics of the upstream solar wind. For more details on natural EM sources and underlying mechanisms, the reader is referred to review papers by Olsen (2007), Constable (2016).

To structure the discussion below, it is practical to divide the spectrum of natural EM variations (Fig. 7) into three frequency bands as listed below. Note that this separation does not strictly follow the physical nature and origin of source currents; rather, it is structured more by how variations in different bands are treated in practice.

3.5.1 Plane-Wave Band

Variations with periods from fractions of a second to several hours will be referred to as the plane-wave or magnetotelluric (MT) band. As soon as one assumes a plane-wave source, a set of MT transfer functions, such as impedance or vertical magnetic field transfer function, can be estimated and used to infer subsurface conductivity. In practice, the impedance transfer function does not require a perfect homogeneous plane-wave source field to remain valid. As long as the source field varies slowly relative to the skin depth, plane-wave impedance remains a valid transfer function and can be used for electromagnetic subsurface sounding. A detailed mathematical justification for this statement was given by (Berdichevsky and Dmitriev 2002; Weidelt and Chave 2012, and references therein). In case of the vertical magnetic field transfer function (often called “tipper” or induction vector) in the MT band, the conditions on the homogeneity of the external source field are stricter. Strictly speaking, under the plane-wave source assumption, local vertical fields in a flat-Earth model can be produced only by lateral subsurface conductivity variations. This is the main reason why estimated tippers are often more prone to so-called source effects (e.g. Araya Vargas and Ritter 2016; Ernst et al. 2020) compared to impedance TFs. The primary reason for these source effects is that any local-to-regional deviations from a perfect homogeneous plane-wave source are likely to generate a radial magnetic field in the external source field (e.g., Jones and Spratt 2002), whereas the plane-wave assumption postulates that the radial magnetic field can only be caused by the horizontal gradients in the subsurface conductivity. For more detailed studies on source effects in MT transfer functions, the reader is referred to recent works by Murphy and Egbert (2018); Sato (2020), Romano et al. (2014), Neska et al. (2018) and references therein. In practice, MT transfer functions are most commonly estimated up to periods of $\approx 10^4$ s, which usually requires few weeks of field measurements. In rare cases, longer recording times are available, thus allowing for the impedance estimation up to periods of few days. The latter is difficult since long measurements of natural electric field variations is a challenge due to low signal-to-noise ratio and electrode instability. Further, at periods longer than 4–5 h special attention must be paid to the presence of non-plane-wave sources such as Sq and tidal signals. To enable the estimation of the EM plane-wave impedance at these periods, a tailored data

processing with a correction for the non-plane wave ionospheric and tidal signals is necessary (Shimizu et al. 2011; Fujii et al. 2015).

3.5.2 Daily Variations Band

Natural variations with periods from several hours to one day will be attributed to the daily band. Dominant natural EM variations in the daily band are associated with the ionospheric current systems with the energy peaking at the daily period and harmonics (Fig. 7). At high and equatorial magnetic latitudes (definition of the geomagnetic coordinate systems induced by the structure of the Earth's magnetic field can be found in Laundal and Richmond (2017)), these signals are mostly driven by the polar and equatorial jet currents. Polar currents get further enhanced and locally dominate the external time variations during magnetically active periods (Finlay et al. 2017; Baumjohann et al. 2010). During magnetically quiet periods, a mid-latitude ionospheric Solar quiet (Sq) variations (Yamazaki and Maute 2017) has been a conventional source of EM induction to constrain the conductivity of the asthenosphere and Mantle Transition Zone (MTZ). In fact, it is Sq variations that were used in the pioneering work by Schuster (1889). Physical phenomena driving the electric currents in the daily band are rather complicated (Richmond and Thayer 2000; Richmond 2017; Yamazaki and Maute 2017), leading to substantial day-to-day, seasonal and annual variability in the geometry and amplitude of the generated magnetic fields. As a result, inducing source currents need to be reconstructed along with the mantle conductivity. This approach was elaborated by Koch and Kuvshinov (2013), Guzavina et al. (2019) who determined complex mid-latitude Sq source currents from data and subsequently inverted for the mantle conductivity. For a spatial basis to describe the Sq source, authors used a small set of SH functions carefully selected following the method proposed earlier by Schmucker (1999). This parameterization works best for the magnetically quiet days around equinoxes at middle geomagnetic latitudes when the Sq source dominates, which implies that only a small portion of data is suitable for the analysis and inversion. A major novelty of the work by Guzavina et al. (2019) was the use of the new global-to-local TFs proposed in Püthe et al. (2015b) and defined in Eq. (32). This approach allows one to take advantage of the TF approach and account for the complex source geometry. More details on this approach will be given below.

A next step forward in this direction was made in recent works by Egbert et al. (2020), Zenhäusern et al. (2021) who derived a physics-based spatial basis using simulations of ionospheric currents from the model of the coupled thermosphere/ionosphere system (TIE-GCM) (Qian et al. 2014). Dominant spatial characteristics of ionospheric currents were extracted from one-year long time series of global TIE-GCM simulations using the Principal Component Analysis (PCA, also known as the method of Empirical Orthogonal Functions – EOF). High spatial and temporal correlation of primary currents enables a compact basis induced by estimated Principal Components (EOFs). In practice, a few tens of basis functions based on EOFs are sufficient to capture over 90% of the global variance in observations. This basis is then used to calculate the equivalent ionospheric source currents following the formalism of the Sect. 3.1.2. The major advantage of this approach is that it allows one to use nearly all data, including measurements from polar regions and those taken during magnetically active conditions. Figure 8 shows equivalent current systems for quiet and active days reconstructed using the physics-based basis and real observations.

It is evident that the Sq current system is visible at mid latitudes on a quiet day, but for a magnetically active day polar currents dominate.

Another EM source in the daily band is oceanic tides. As will be discussed in Sect. 4.2, this source was proven feasible for imaging the conductivity of the sub-oceanic upper mantle. For this source, the extraneous current density, \vec{j}^{ext} , is confined to the water column and in frequency domain can be written as

$$\vec{j}^{\text{ext}}(\vec{r}, \omega) = \sigma(\vec{u}(\vec{r}, \omega) \times \vec{B}(\vec{r}, \omega)), \quad (49)$$

where σ is the electrical conductivity of seawater, $\vec{E}, \vec{B}, \vec{u}$ is the fluid velocity. Unlike in other conventional EM induction methods, where sources are coupled to the subsurface inductively, here currents form within the ocean (where $\vec{u} \neq 0$) couple to the ocean bottom both galvanically and inductively (Minami 2017; Zhang et al. 2019). Next to the core, oceans is the only other region with the bi-modal EM coupling to the solid Earth. Since induced magnetic fields are small compared to the amplitude of the total ambient magnetic field, we can assume $\vec{B}(\vec{r}, \omega) \equiv \vec{B}^{\text{core}}(\vec{r})$ in the equation above, where \vec{B}^{core} is a core field model. Another key difference from ionospheric and magnetospheric sources is that all components needed to represent the extraneous current due to oceanic tides are known to a good degree, including the ocean velocities provided by assimilated satellite altimeter data (Stammer et al. 2014) and core field models (Alken et al. 2021). Many other details on how to best discretize and represent motionally induced sources in order to achieve the best performance and accuracy in the context of 3-D EM simulations were discussed by Velínský et al. (2018). We also note that the tidal magnetic signals are a potential source of noise for studies where ionospheric currents are used (Schnepf et al. 2018; Yamazaki 2022). If the quality and length of observations do not allow for spectral and spatial separation of ionospheric and tidal components, a generally better known oceanic tidal magnetic field can be simulated and subtracted following the approach of Guzavina et al. (2018).

3.5.3 Long-Period Band

Finally, the third band covers periods between few days and a solar cycle. In the literature, EM variations at these periods are often considered to be induced by magnetospheric current systems. It is probably justified to say that the magnetosphere is the dominant source region in the long-period band. However, variations induced at annual and seasonal periods due to changes in the ionospheric current systems and persistent ionosphere-magnetosphere coupling (Richmond and Thayer 2000; Richmond 2017) will also result in variations in the long-period band. Therefore, such separation based solely on the temporal condition is not correct.

The axisymmetric component of long-period band currents is conventionally described by the first zonal SH function (P_1^0), and its origin is attributed to the magnetospheric ring current (RC). Under some (often omitted) assumptions, one can use variations described by the P_1^0 SH coefficients to estimate both local and global C_1 and Q_1 responses as defined in Sects. 3.3–3.4. In the last two decades, several space missions (THEMIS, Van Allen Probes, Cluster II, MMS, among others) allowed for measuring the magnetic field and plasma parameters directly within the magnetosphere. These data led to the construction of elaborate data-constrained models of the magnetosphere (e.g. Tsyganenko 2013) and advanced our understanding of different current systems in the magnetosphere (Baumjohann et al. 2010; Ganushkina et al. 2018). Next to their complex geometry, numerical models and observations also reveal dynamic coupling between different magnetospheric

current systems. Since current-generating regions are at least few Earth's radii away (with the exception of the polar region, where magnetosphere and ionosphere are coupled through the field-aligned currents) from the Earth's surface, most small-scale effects attenuate. Therefore, superposed magnetic field of the magnetospheric origin that we observe on the ground or at LEO satellites is generally large scale, yet assuming it can be fit by the first zonal harmonic alone is not reasonable and most recent global EM models (e.g. Püthe et al. 2015a; Grayver et al. 2017; Kuvshinov et al. 2021; Velímský and Knopp 2021) stand to rectify this problem by including more spatial terms to describe the inducing field. It remains to be shown whether physics-based models of the magnetosphere can be used to improve the source parameterization adopted in EM induction studies as has been shown for the ionospheric daily band variations (see discussion above).

Next to a higher spatial complexity inherent to the magnetosphere, it has long been known (Olsen 1999b; Kuvshinov and Semenov 2012) that long-period TFs can be biased if the magnetic field is observed in regions where strong signals from other, mostly ionospheric, electric current systems are present. The problem occurs because very dynamic and small-scale high-latitude and equatorial current systems (such as due to Equatorial, Polar and Auroral Electrojets) cannot be resolved with a sufficient spatiotemporal resolution by the current observational network. Limited local-time and/or spatial coverage presently do not allow for a sufficiently detailed data-based description of these current systems. Therefore, magnetic field effects due to unresolved currents appear as a systematic correlated noise in the data, which often leads to biased magnetospheric transfer functions independent of the frequency. Exclusion of data at high-latitude and equatorial geomagnetic latitudes cannot fully rectify this problem since the magnetic field due to polar currents easily reaches mid-latitude regions. To minimize a potential bias of the magnetospheric transfer functions by polar currents, several approaches have been proposed in the past decade. In the most general case, high-latitude currents can be co-estimated along with the magnetospheric magnetic field as is done in the Comprehensive Inversion models (Sabaka et al. 2018, 2020) where many different sources are co-estimated simultaneously. In Martinec et al. (2018), the authors proposed a dedicated along-track filtering of the Swarm magnetic field residuals that aims to mitigate the contaminating effect of high latitude currents. This approach was further developed by Martinec and Velímský (2022) who show that in addition to the SH-based representation of the magnetospheric field, co-estimating ionospheric currents as elementary loop currents reduces the ionospheric contamination. In Sun et al. (2015), authors determine ionospheric currents as a part of the mantle conductivity inversion scheme and account for the effect of unresolved ionospheric signals through non-trivial data covariance matrix, where ionospheric currents are iteratively re-estimated in form of a correlated noise component.

To illustrate the issue with the reliance on the zonal current assumption in C_1 responses estimated at the ground magnetic field observations using the Z/H method (see Sect. 3.4), I will carry out the following experiment. Let us take a set of quality-controlled measurements of the hourly mean vector magnetic fields (Macmillan and Olsen 2013) for the period between 2013–12–01 and 2019–11–01. The model of the core and crustal fields as given by the Comprehensive Inversion (CI) model (Sabaka et al. 2018) was subtracted from this data such that the variations in the remaining data set are mostly driven by the mid-latitude ionospheric and magnetospheric current systems. Observatories poleward of the 56° and equatorward of 5° geomagnetic latitudes were excluded to minimize the contaminating effect of polar and equatorial current systems, resulting in 50 – 110 observatories over the globe depending on time. The vector magnetic field is transformed into the Geomagnetic reference frame (Laundal and Richmond 2017) to better approximate large-scale

magnetospheric current systems. Next, SH coefficients of external and internal origins are estimated within each time window using a robust least-squares method for SH models of varying complexity. In the simplest case, external field is described by a single zonal SH coefficient (i.e. P_1^0 assumption of the Z/H method) in a time window. Alternatively, magnetic field observations are expanded using all SH functions up to the degree 2 or 3, giving 8 and 15 terms, respectively. For each time window, a coefficient of determination is calculated (R^2 statistics, also referred to as squared coherency) and daily mean values of these coefficients are plotted as time series in Fig. 9 for all three models of the external field. Corresponding Cumulative Distribution Function estimate plots for all hourly time windows and three models are given in the inner plot.

It is evident that the model based on the first zonal harmonic is able to fit only a small fraction of the total signal variance, in 10% of the time windows the $R^2 \leq 0.1$, and $R^2 < 0.5$ for more than half of time windows. Therefore, P_1^0 coefficient is not a dominant spatial mode for the majority of time. In contrast, models based on the SH expansions up to the degree 2 and 3 systematically explain more variance in the observed magnetic field variations. Going to a higher SH degree creates a risk of data over-fitting, hence the models are limited to the SH degree 3. This experiment shows that using the P10 assumption to describe long-period magnetic field variations observed at a given location (i.e. geomagnetic observatory) is generally not justified and should be avoided in favour of more advanced techniques that allow for a more realistic source description. This is particularly relevant for 3-D inversions based on the Z/H method (equivalently, C_1 or GDS responses from Eq. 48) where generally very small EM effects from plausible conductivity variations in deep mantle are most likely overshadowed by source effects due to non-P10 source terms, resulting in non-physical subsurface conductivity variations. This issue is far less severe in case of global average conductivity models since localized source effects are partially averaged by deriving a global response from the observatories over the globe.

In summary, methods that allow one to incorporate more realistic models of the external source and reduce the effect of ionospheric currents, should always be preferred to conventional techniques (e.g. those described in Sect. 3.4).

3.6 Forward Modelling

Modelling EM variations due to global spatially heterogeneous sources requires dedicated tools and methods. For MT and near-surface studies, it is conventional to work with a flat-Earth model, whereby part of the spherical surface (with a geodetic reference datum) is projected onto a plane using an arbitrary geographic projection and the modelling/inversion is then carried out in a local Cartesian coordinate system. For large-scale EM studies ($L > 10^3$ km, where L is a characteristic length representing the source, survey scale or skin depth), one needs to resort to spherical coordinates and work in a sphere, spherical shell or a part thereof, assuming electrical conductivity varies in all three dimensions (Fig. 5). For modelling purposes, extraneous currents are typically represented using an equivalent current density that can be parameterized using (a combinations of) volumetric currents, dipoles, loops or thin sheet currents (see Sects. 3.1.1–3.1.2). As for the Cartesian case (i.e. under the flat-Earth assumption), analytical solutions of Eq. 11 are generally available only for cases where the conductivity varies in the radial direction, that is $\sigma(\vec{r}) \equiv \sigma(r)$. In presence of lateral variations, governing PDEs are solved using numerical methods.

In a benchmark paper by Kelbert et al. (2014), the status of global EM induction modelling has been discussed in details, presenting all actively used and developed codes at

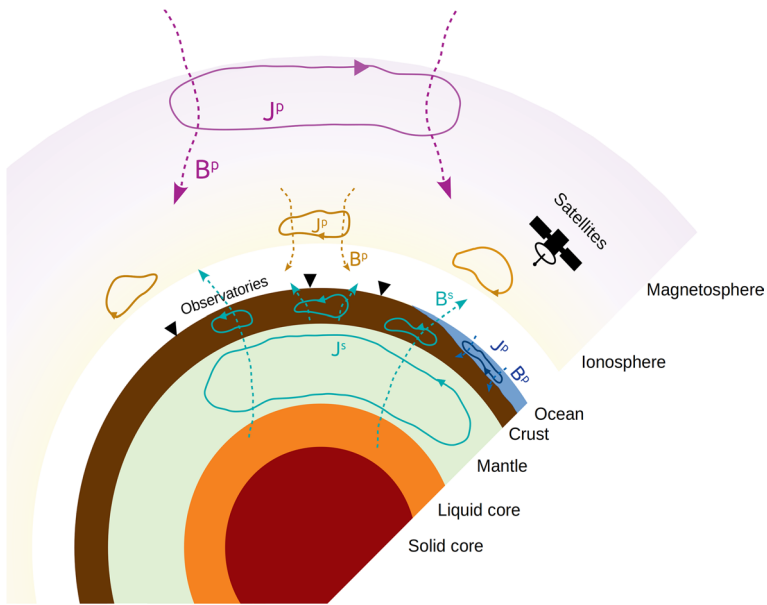


Fig. 5 Principle of electromagnetic (EM) induction. Primary magnetic field (\vec{B}_p) induced by primary current density J_p , which exist in the exterior (mostly in the ionosphere-magnetosphere system) or within the oceans. Secondary currents (\vec{J}_s) and fields (\vec{B}_s) are induced in the Earth’s interior by virtue of EM induction

Table 3 Summary of deep electromagnetic sounding methods

Method	Source region	Model of the source	Data sources	Sounding depths (km) ¹
Magnetotellurics (MT)	Ionosphere, lower atmosphere	Plane wave	Temporary stations/ arrays	0–350
GDS ²	Ionosphere	Equivalent current sheet	Temporary stations, geomagnetic observatories, satellites	200–600
	Magnetosphere	Equivalent current sheet	Observatories, satellites	400–2600
Tidal	Oceanic tides	Oceanic tidal models	Satellites, seafloor temporary stations	10–400

¹Given values are first-order approximations. In reality, this depends on many factors including subsurface conductivity, source geometry (Fig. 6) and data quality

²GDS stands for Geomagnetic Depth Sounding

that time. All participating codes were tested on a set of conductivity and inducing source models of varying complexity. This review is still relevant and reader can find many details about status of global forward modelling, yet the last decade has had several important developments, which will be followed in the future. First of all, a new generation of codes has been developed. This includes a revised finite-difference code (Zhang et al. 2019), new finite-element (FE) codes (Grayver et al. 2019; Yao et al. 2022; Wang et al. 2023), further developed mixed spectral-FE (Velímský et al. 2021, 2019, 2018) and integral equation

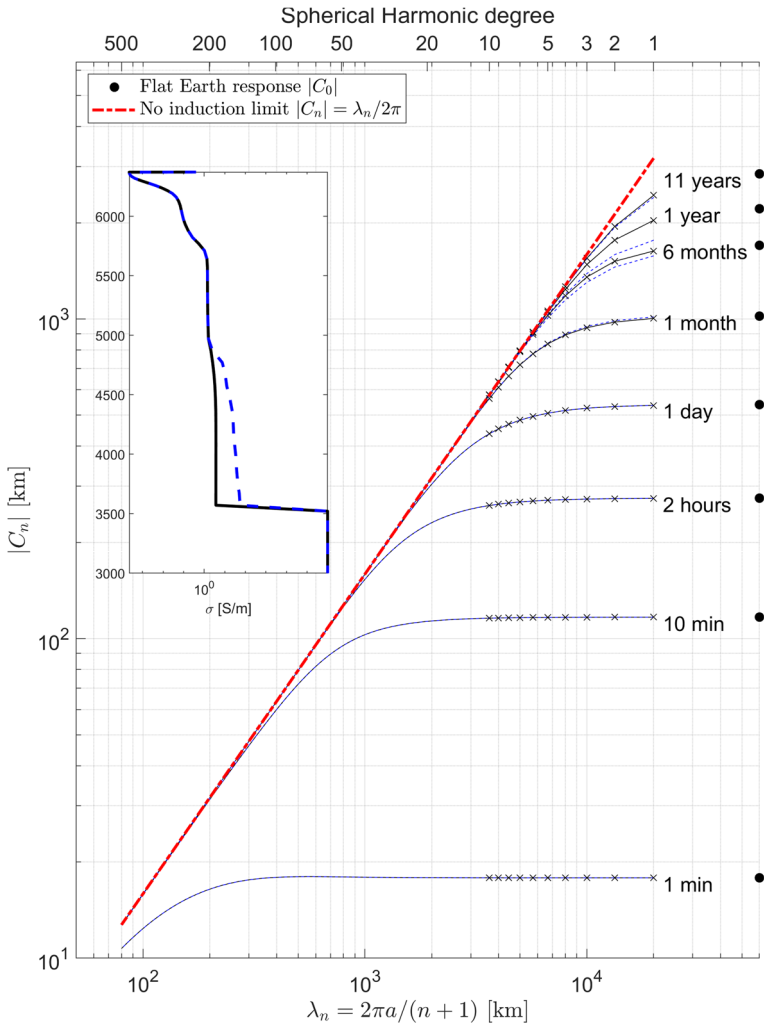


Fig. 6 Absolute value of the C -response transfer function (see Sects. 3.3–3.4 for the definition) for two 1-D radial conductivity models (shown in the inset) as a function of horizontal scale-length λ_n and period (curves correspond to periods from 1 min to 11 years) of the external field source. Dashed blue lines are for the conductivity model with a more conductive lower mantle. Recreated with modifications after Olsen (2007)

solutions (Kruglyakov and Kuvshinov 2022; Sun and Egbert 2012). With the exception of Velínský et al. (2021), all codes solve governing equations in the frequency domain. However, computationally efficient approaches for adapting frequency domain codes to time domain problems have also been presented (Grayver et al. 2021; Kruglyakov et al. 2022).

Another development in the field was motivated by the advent of continental MT surveys discussed in Sect. 2. Conventional 3-D MT solvers all operate under a flat-Earth assumption. However, assuming that Earth is flat for surveys that span entire continents is not physical and can lead to erroneous EM responses resulting from distorted geographic

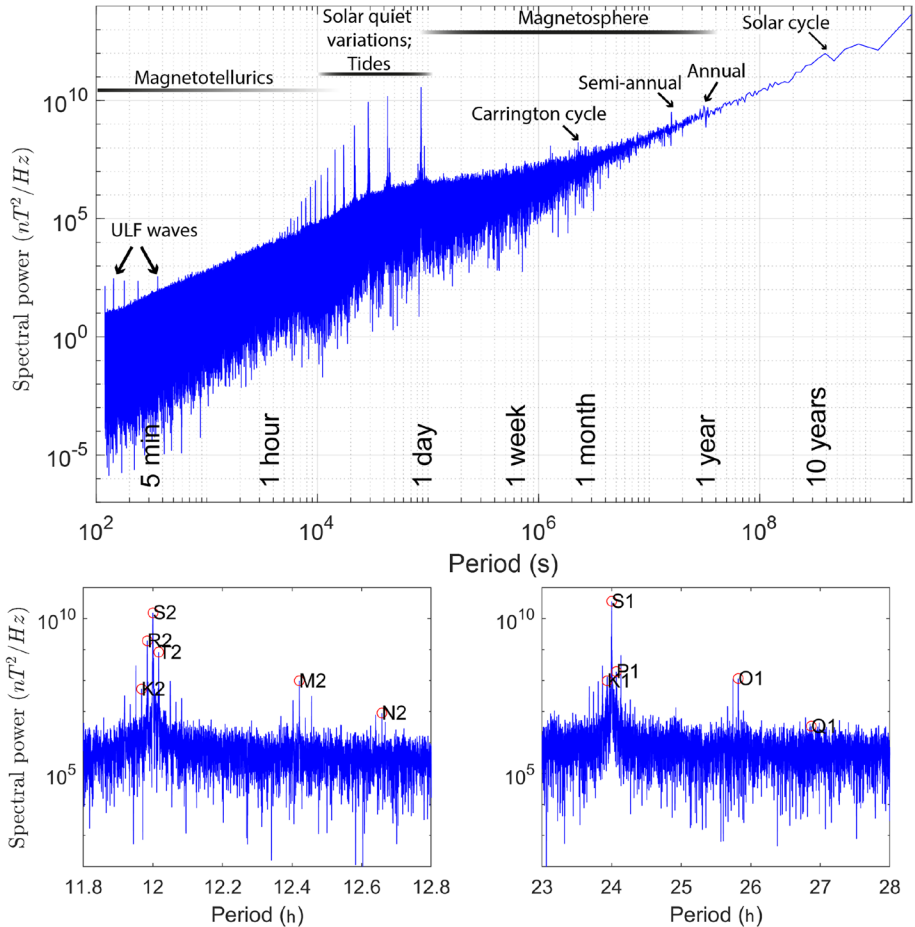


Fig. 7 Top: Amplitude of radial magnetic field components measured at the Honolulu/USA geomagnetic observatory between years 1945 and 2019 for periods between 2 min and 30 years. Some of the major sources and designated bands are denoted. Bottom: Zoomed in spectrum around 12 and 24 h. Red circles are plotted at periods of major lunar and solar tidal constituents

projections if such distortions are not explicitly accounted for. This motivated the development of a new type of MT solvers that operate in the spherical frame rather than in a flat Cartesian model. In addition to changing the reference coordinate system, this required development of a new source model that, once imposed on a spherical shell, would produce valid MT transfer functions. New 3-D MT forward solver with an adapted source model for the impedance tensor has been presented by Grayver et al. (2019). The source model used in this work is based on a combination of orthogonal uniform planetary fields represented by SH functions of degree one (Eq. 31), and works for the impedance tensor, but not for “plane-wave” induction vectors (“tippers”). An alternative solution based on uniform meridional currents has been developed by Kruglyakov and Kuvshinov (2022). Although more technical, this approach also allows one to model “plane-wave” induction vectors for a 3-D conducting spherical shell. A comparative study on modelling MT in spherical and projected Cartesian plane systems was presented by Han and Hu (2023).

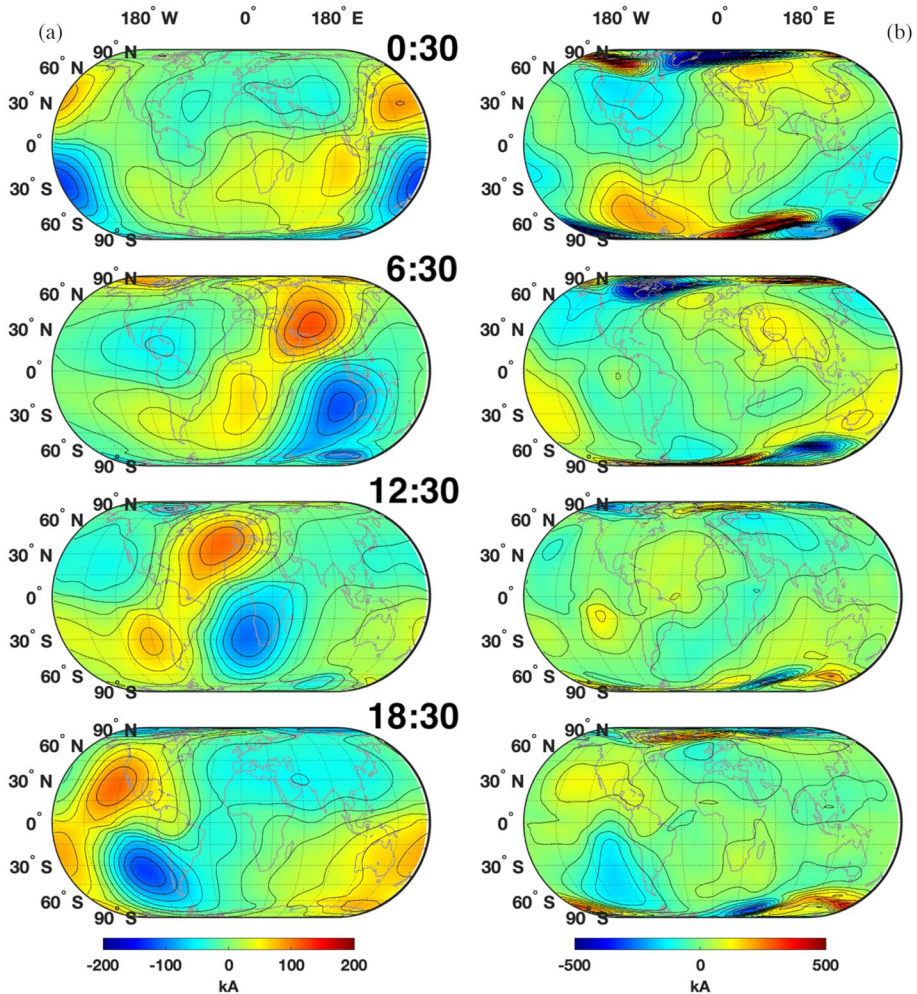


Fig. 8 Physics-based estimated equivalent sheet current stream functions, showed at 6 hr intervals (UT), for two days: **a** 9/24/2002, a quiet day. **b** 10/02/2002, near the start of a magnetically active interval. Units of the stream function are kAmp; note that different colour scales were used for the two days. Figure modified after Egbert et al. (2020)

One of the major challenges in EM induction is the ability to model EM phenomena across a broad range of periods (Fig. 7) and accurately represent local conductivity gradients (e.g. due to the coastline). These challenges demand multi-scale modelling approaches. The most efficient way to address this challenge is to use locally refined meshes. This is most easily achieved when the finite-element method (FEM) is invoked (an example of such meshes is shown in Fig. 10), where by refining individual elements a smaller length-scales can be modelled more accurately within regions of interest. Importantly, the numerical solution of governing equations obtained with the FE method remains globally conservative and retains all asymptotic convergence properties upon local refinement (Bangerth and Rannacher 2003). A similar “multi-scale” modelling capability can be achieved with a nested-IE approach presented by Chen et al. (2020), although this approach involves some

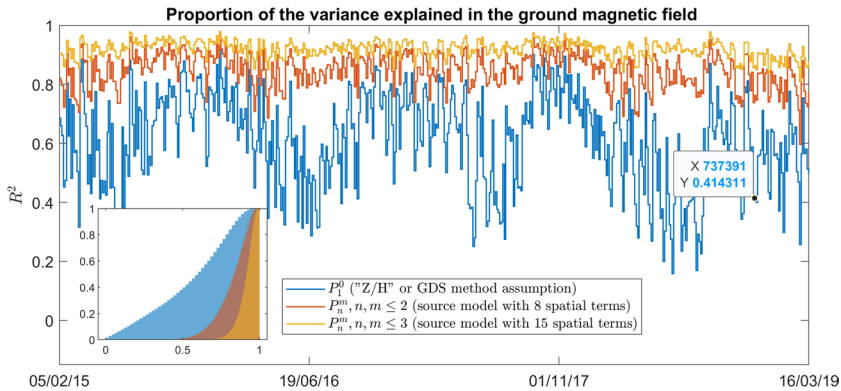


Fig. 9 Daily averages of the R^2 coefficient for three models based on the SH expansions of the magnetic field hourly means as measured by a global network of ground magnetic observatories. The inner plot shows Cumulative Distribution Function estimate for all three models

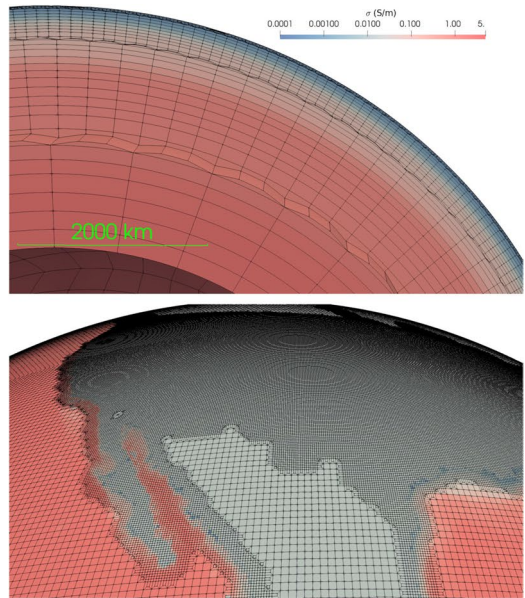
ad-hoc choices and it remains to be shown if the resulting scheme is globally conservative and asymptotically convergent. Another major trend is related to adding a support for modelling only part of a sphere (Grayver et al. 2019; Zhang et al. 2019; Yao et al. 2022). This is practical when working on a continental scale and at periods where considering the entire planet is not necessary (Fig. 6). Modelling domains that constitute only part of a spherical shell (or sphere) are straightforward for FD/FE codes since these methods are based on local basis functions and allow one to impose arbitrary boundary conditions, whereas IE and spectral codes need to operate globally in order to retain their computational efficiency.

3.7 Inversion

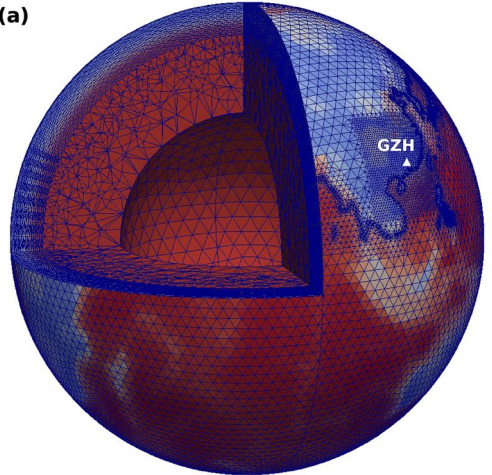
In general, neither the inducing source current density \vec{j}^{ext} nor subsurface conductivity σ (cf. Eqs. 10–11) are known. Therefore, in the most general case, our inverse problem seeks estimates of both source and subsurface conductivity variables. In some cases, one can reduce the problem and remove the unknown source term. For instance, assuming a plane-wave source geometry, substituting this into equation 12 and doing some algebra (Berdichevsky and Dmitriev 2002; Weidelt and Chave 2012) allows one to obtain MT transfer functions, which are independent of the instantaneous amplitude of source current term. Another exception are oceanic tidal sources, where the inducing current can be constructed based on the independent models (see Sect. 3.5 for more details). Local C_n responses (Eqs. 44–45) can also be used to eliminate the source term by assuming that the source geometry is described by a single known SH harmonic function. The limitations and consequences of this rather strong and often unrealistic assumption have already been discussed in previous sections.

In the past decade, main developments in large-scale (global) EM inversion methods were concentrated around three points: (i) implementation of inverse solvers based on new forward operators discussed in the previous section; (ii) development of inversion codes where more realistic inducing source models are allowed and subsurface conductivity can be estimated simultaneously with an inducing source model, and (iii) development of

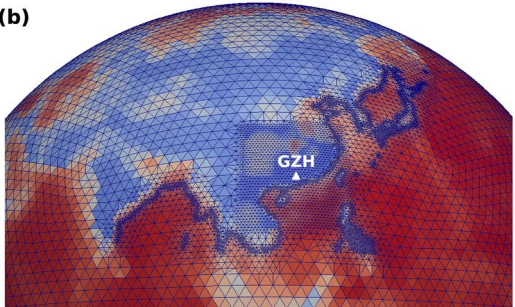
Fig. 10 Top: locally refined multi-scale hexahedral (top) and tetrahedral (bottom) meshes from Grayver et al. (2019) and Yao et al. (2022), respectively



(a)



(b)



probabilistic/stochastic approaches that assign a notion of uncertainty to retrieved subsurface conductivity models.

As is the case with other electromagnetic inverse problems, the conventional way to solve a large-scale (global) EM inverse problems is by minimizing a regularized objective function of the following form

$$\min_{\mathbf{m}} \left[\frac{1}{2} \left\| \mathbf{d}^{\text{obs}} - \mathbf{d}^{\text{mod}} \right\|_{\mathbf{C}_d^{-1}}^2 + \frac{\gamma}{2} R_m(\mathbf{m}) \right], \quad (50)$$

where \mathbf{m} is a vector of unknown model coefficients that parameterize the subsurface conductivity, \mathbf{C}_d is a data covariance matrix and $R_m(\cdot)$ is a regularization operator on \mathbf{m} . The modelled data vector $\mathbf{d}^{\text{mod}} = \mathbf{F}(\mathbf{m})$ entails solving a forward problem.

In case of computationally expensive 3-D forward operators and high-dimensional model spaces, minimization of the objective function (50) is typically done by means of derivative-based optimization methods, which require calculation of the gradient (and possibly Hessian) of the forward operator. The most efficient way to obtain derivatives of a high-dimensional PDE-constrained operator is by using the so-called adjoint method. In Egbert and Kelbert (2012), Pankratov and Kuvshinov (2015), authors present a general formalism for computing the gradient and Hessian of the objective function for EM induction problems using the adjoint-based approach. These works focused on governing equations formulated in the frequency domain for ground-based observations. The work of Maksimov and Velímský (2017) presented efficient calculation of the gradient and Hessian for time domain global problems, which can incorporate both ground and satellite data (Velímský and Knopp 2021). Further, Püthe and Kuvshinov (2014) presented an adjoint-based method for the inversion of the global Q -matrix responses (Sect. 3.3). The latter can be estimated from the ground and satellite data (e.g. ESA Swarm) and was inverted for 3-D conductivity distribution in the mantle by Kuvshinov et al. (2021).

Adjoint-based approaches are not only important for “optimal” navigation in the high-dimensional model space in derivative-based optimization methods, but also serve as a basis for efficient uncertainty quantification (UQ) where knowledge on local objective function derivatives is essential to make the problem of UQ computationally tractable (Ren and Kalscheuer 2020). In addition to the UQ accelerated by exploitation of the gradient/Hessian, more conventional probabilistic inversion schemes were developed, although these approaches are mostly limited to low-dimensional 1-D problems with inexpensive forward operators. Püthe et al. (2015a), Verhoeven et al. (2021), Yao et al. (2023b) posed global EM inversion using the Bayesian formalism and sampled the corresponding posterior Probability Density Function (PDF). For this task, all used a 1-D forward operator (i.e. conductivity model is assumed to vary only in the radial direction) and derived a global average conductivity profiles using ground and satellite data. A set of inversion codes based on stochastic optimization methods were also developed to mitigate limitations of the derivative-based methods yet allow for a more physically realistic forward operator. Grayver et al. (2016), Chen et al. (2022) inverted ground and satellite long-period EM responses using a stochastic optimization method called Covariance Matrix Adaptation Evolution Strategy (CMAES), which can find global minima and provides an ensemble of equivalent data-fit models as a rough model uncertainty estimate. In these schemes, the mantle was still parameterized using a 1-D radial profile, but a heterogeneous conductivity layer was added on top to model 3-D induction effects due to realistic ocean bathymetry and sediment cover since these effects are often too significant to be neglected. In the next decade, we will likely see new probabilistic inverse codes that take an advantage of adjoint-based gradient

and Hessian operator with full 3-D physics and can sample high-dimensional model spaces in a reasonable amount of time (Fichtner et al. 2021; Zhao et al. 2022; Zhang et al. 2023b).

As was alluded to at the beginning of this section, generally neither the inducing source nor the subsurface conductivity are known. In the rest of this section, we therefore discuss the development of methods where both the source structure and subsurface conductivity distribution are estimated simultaneously from the data as parts of a single inverse problem. For this purpose, the minimization problem in Eq. (50) is expanded into the so-called separable nonlinear least-squares (SNLS) problem, which reads

$$\min_{\mathbf{m}, \mathbf{c}} \left[\frac{1}{2} \left\| \mathbf{d}^{\text{obs}} - \mathbf{d}^{\text{mod}} \right\|_{C_d^{-1}}^2 + \frac{\gamma}{2} R_m(\mathbf{m}) + \frac{\gamma_c}{2} R_c(\mathbf{c}) \right]. \quad (51)$$

Here, in addition to unknown subsurface conductivity parameters \mathbf{m} , the problem also seeks an estimate for the source coefficients \mathbf{c} and $\mathbf{d}^{\text{mod}} = \mathbf{F}(\mathbf{m})\mathbf{c}$. The key characteristic of this form is that while the problem is nonlinear with respect to the conductivity, it is linear relative to the source coefficients. This property of the SNLS problem allows us to devise efficient solution strategies (Min and Grayver 2023).

Many recent studies (Koch and Kuvshinov 2013; Sun et al. 2015; Guzavina et al. 2019; Egbert et al. 2020; Zhang et al. 2022) have adopted a so-called alternating approach to solve the problem (51), whereby the source structure is estimated given some prior knowledge about the subsurface conductivity. With this estimated source structure, the inversion in terms of subsurface conductivity is subsequently performed and the updated conductivity model can again be used to re-estimate the source coefficients. Such separate estimation of the two model spaces is assumed to result in progressively refined knowledge of both the source and conductivity models. The alternating approach outlined above is the simplest way of solving a SNLS problem. However, it does not enforce consistency between conductivity and source models and may suffer from the slow convergence. In Min and Grayver (2023), authors explored more efficient ways of solving the SNLS problem. Namely, they implemented the variable projection method (VP), which has been proposed as an optimal method for solving SNLS problems in other domains (O’Leary and Rust 2013). The VP method benefits from both computational efficiency and fast convergence. In essence, VP exploits the linear dependency in one part of the model and estimates this part via linear least squares at each iteration, thus optimally (in a least-squares sense) projecting the complete model space onto a reduced subspace for efficient nonlinear optimization. The key advantage of the approaches listed above is that one does not rely on oversimplified assumptions about the source structure (as happens, for instance, in the inversion of C_1 responses), but can estimate a more complex and realistic source model directly from the data. On the other hand, this implies that the problem has even more unknowns.

4 Case Studies

4.1 Plane-Wave Band

As was discussed in Sect. 2, the advent of national-wide MT arrays unlocked unprecedented opportunities for the MT imaging. However, before discussing research based on these data, we will briefly look at studies where modern tools were used to reprocess and model legacy data from older large-scale arrays. A good example is the AWAGS array

of ≈ 60 magnetometers, which recorded magnetic field variations over the Australian continent for nearly one year in 1989–1990. Wang et al. (2014) derived induction vectors for stations from the AWAGS array using a modern robust processing code and inverted them for a 3-D conductivity structure beneath Australia. The authors obtained a model that fits the data and contains conductivity variations that correlate with some major geologic structures. In the next decade, we can expect more on the imaging of the 3-D conductivity under the entire Australia with the AusLAMP array that presently is half-way through to its completion (Fig. 2).

Kelbert et al. (2019a) presented the USArray-based conductivity model for the contiguous US. The model is a compilation of several regional conductivity models derived using subsets of the USArray data. In areas outside of the USArray, the global conductivity model by Sun et al. (2015) was used. In this work, the authors attempted to create a coherent 3-D conductivity model to constrain the location and extent of electrical structures due to various geologic structures traversing the contiguous US. Murphy et al. (2023) has updated the model by re-inverting overlapping subsets of USArray using common inversion settings, which improved the spatial coherency of the compiled continental 3-D model. Yang et al. (2021) inverted a subset of ≈ 450 USArray stations imaging large-scale conductivity variations under contiguous US and inferred an average water content of the asthenosphere needed to explain recovered conductivity structure. Notably, they found that using a starting model derived from the global 3-D conductivity model by Kelbert et al. (2009) results in more plausible conductivity variations within the asthenosphere. Another 3-D inversion of the USArray was performed by (Singh and Dehiya 2023) within a broader methodological study.

Most recently, Munch and Grayver (2023) performed a 3-D inversion of nearly 1300 MT stations from USArray to derive a multi-scale model of electrical conductivity for the conterminous US. Retrieved conductivity variations in the asthenosphere were interpreted in terms of lateral variability in the water content of the Olivine phase. To this end, a joint seismic-EM interpretation was performed, whereby seismic velocity and conductivity were linked through the thermodynamic phase equilibria modelling. As a starting model, an adapted global average satellite-based conductivity model of Grayver et al. (2017) was used to guide the 3-D inversion. This is the first study where 3-D MT inversion was performed directly in the spherical frame, that is without invoking the flat-Earth assumption and thus avoiding any geographic projection. It is likely that more studies will adopt a more natural spherical frame in the future, provided needed technical developments (see Sect. 3.6) are in place.

Next to fundamental questions related to the structure of the crust and mantle, it was already demonstrated that these models play a major role in identifying and imaging the source rocks of mineral systems (Kirkby et al. 2022) and are indispensable for assessing the impact of Space Weather events on the ground infrastructure (Kelbert 2020; Murphy et al. 2021). Significant new developments and advances in these directions can be anticipated as the extent of surveys and quality of continental-scale EM imaging improve.

4.2 Oceanic Sources

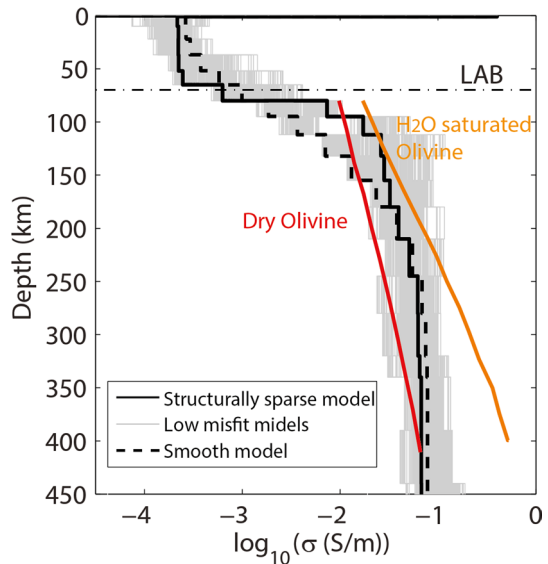
Tidal motion of the electrically conducting seawater in the oceans produces a time-varying magnetic field signal by means of a phenomena called motional induction. The physical aspects and historical works aimed at studying these phenomena were thoroughly covered in the recent EM review by Minami (2017). In this section, we will describe the progress

that has been enabled through the usage of tidally induced magnetic signals for probing electrical conductivity of the mantle below oceans. This development is one of the most significant methodological breakthroughs of the last decade in the field. Given logistical hurdles and cost of marine EM surveys, tidal magnetic signals mapped globally by satellites is practically the only natural signal in the relevant period range that can be used to study electrical conductivity of the sub-oceanic mantle on the global scale, and will help us better understand processes that occur at and close to the lithosphere-asthenosphere boundary.

The first successful attempt to globally map the weak magnetic tidal signal due to the lunar principal semi-diurnal tidal constituent (M_2) was based on a few years of magnetic field observations from the CHAMP mission (Tyler et al. 2003). The application of this signal for mantle sounding was not envisioned at that time, although this work demonstrated the remarkable high quality of satellite magnetic data. The next major step forward was the release of the Comprehensive Model (CM5) by Sabaka et al. (2015). It retrieved the global magnetic field due to the M_2 magnetic tidal signal with the quality that was sufficient to use it for probing the electrical conductivity of the upper mantle beneath the oceans. This was first demonstrated in a forward modelling study by Schnepf et al. (2015). Later, a full inversion code was developed by Grayver et al. (2016) who applied it to map the global average conductivity structure of the oceanic upper mantle. These papers demonstrated the feasibility of using satellite-detected magnetic tidal signals as an electromagnetic induction source for imaging the upper mantle below the oceans (Fig. 11), which previously was only done using locally measured EM signals. The works of Grayver et al. (2016), Saynisch et al. (2018) also ran detailed error propagation studies, showing how different input variables used for construction of the ocean tidal current density propagate to the simulated magnetic fields.

The CM5 magnetic field model was constructed using pre-Swarm satellite magnetic observations, namely Ørsted, CHAMP, and SAC-C missions. The launch of the Swarm satellites by ESA pushed this field to the next level by enabling the calculation of East–West gradients due to the orbital configuration whereby Swarm A and Swarm C spacecrafts fly at a small longitudinal separation. Among other advantages, this enabled an improved determination of the M_2 signal (Sabaka et al. 2016, 2018). Collection of additional data has enabled global mapping of other weaker tidal constituents, such as N_2 and O_1 by Grayver and Olsen (2019). The O_1 is particularly useful in the context of the mantle conductivity studies because its period (25.82 h) is roughly twice longer than that of the M_2 constituent (12.42 h), adding sensitivity to the deeper asthenosphere. Subsequent studies also extracted the three mentioned constituents using other data processing and magnetic field separation approaches (Sabaka et al. 2020; Saynisch-Wagner et al. 2021). All mentioned papers parameterized tidal magnetic signals using truncated series of SH functions. Current observations and state of data processing and calibration impose restrictions on spatial resolution of the tidal magnetic field models. For instance, the dominant M_2 constituent was reliably characterized up to the truncation degree of $n \leq 30$, implying the spatial resolution of ≈ 1000 km. Magnetic signals due to other weaker constituents have a lower spatial resolution. A dedicated modelling study by Velínský et al. (2018) showed that the spectrum of tidal magnetic signals decays exponentially with the SH degree, thus estimation of signals at higher SH degrees is increasingly challenging. Next to the improved data processing workflow, a major boost in spatial resolution of extracted tidal magnetic signals will likely be achieved at the end of life of ESA Swarm satellites, namely when spacecrafts will go on lower orbits prior to reentering the atmosphere eventually. This short period, informally called the “mapping phase”, will be a favourable window for characterization

Fig. 11 Black solid and dashed lines represent the most probable models obtained by using structurally sparse (that is, permit conductivity jumps but allow as few features as possible) and smooth constraints in the inversion algorithm, respectively. The grey lines denote the 1000 models for which misfit differs by no more than 10% relative to the most probable solution. Conductivities of the dry and water-saturated Olivine are shown with red and orange lines, respectively. Figure modified after Grayver et al. (2016)



of small-scale magnetic fields due to oceanic tides or crust/lithosphere. It is planned that the Swarm A/C spacecrafts will enter this “mapping phase” during the next solar minimum when the effect of contamination due to ionospheric and polar current systems will be the lowest.

Next to retrieval of ocean tidal magnetic signals from satellite data and their use in a global conductivity inversion, there were also successful attempts to use tidal magnetic signals registered at ocean-bottom EM instruments (OBEM). In Zhang et al. (2019), the authors used an array of OBEM instruments and derived a conductivity model of the sub-oceanic upper mantle beneath a region in the Pacific ocean using locally measured tidal magnetic signals. Interestingly, tidal signals are normally considered noise and filtered out in marine EM studies. A key message of this study is that tidal magnetic signals can add value when combined with local MT transfer functions, which are usually the main purpose of deploying OBEM stations. The advantage of OBEM measurements compared to satellite data is of course their higher sensitivity to the mantle, both because they are close, but also because magnetic signals measured within the ocean contain both poloidal and toroidal components, whereas only the poloidal part of the magnetic field can be measured at a satellite (Velímský et al. 2019). However, sparsity of OBEM measurements limits their application to a few regions worldwide.

All studies mentioned above parameterized the oceanic mantle using a 1-D radial conductivity model. The layer on top, representing ocean and sediments was parameterized as a thin layer of equivalent laterally variable conductance. A major methodological development was undertaken by Šachl et al. (2022), where authors developed a new 3-D inversion scheme for tidal magnetic signals. Their results show that magnetic signals detected by LEO satellites can indeed be used to invert for the 3-D electrical structure of the upper oceanic mantle, provided tidal magnetic signals of sufficient accuracy and resolution are in place. In a related earlier study, Martinec et al. (2021) constructed a new integrated geophysical-petrological global 3-D model of the upper-mantle electrical conductivity and

validated it by the M_2 tidal magnetic field as given by Sabaka et al. (2018) and Grayver and Olsen (2019).

The global tidal magnetic signals have also been used in combination with long-period magnetospheric variations to enable sensitivity across a larger range of depths. Some research output on this topic is described in Sect. 4.5.

One further development that aimed to aid a more accurate modelling of motionally induced signals is a more realistic physical representation of the ocean and marine sediments within the model. Conductivity of the ocean and sediments is usually assigned a priori and this part of the model remains fixed. Given that both the ocean and porous marine sediments are prominent 3-D conductors, more faithful representation of these layers is important because inducing and induced EM fields propagate and get distorted by complex 3-D induction effects that occur in the ocean and sediments. The most common approach has been to use an arbitrary constant value for the seawater and sediments (the latter are often neglected despite their total conductance can be even higher than that of the overlying ocean). A significant step forward has been made by using observations of seawater salinity and temperature to compute physics-based 3-D conductivity models of the ocean and marine sediments. This has been enabled by using validated climatology products from the World Ocean Database or interpolated grids given by the World Ocean Atlas (WOA) together with the thermodynamic Equation of State for seawater. Tyler et al. (2017) derived a 3-D conductivity model of the global ocean with the resolution of 1° . Subsequently, a $1/4$ degree resolution product was added as a part of the WOA (Reagan et al. 2019). Independently, Grayver (2021) derived an atlas of the world ocean and marine sediments electrical conductivity by combining global and regional ocean climatologies and a recent global model of marine sediments thickness (Straume et al. 2019). Figure 12 shows an example from two of the published models. These elaborate ocean and sediments conductivity models are also instrumental for regional MT inversions, global EM induction studies, and modelling of surface electric fields for GICs in the coastal areas.

4.3 Daily Variations Band

Daily band variations of the magnetic field are mostly produced within the ionospheric dynamo regions (Olsen 2007; Yamazaki and Maute 2017). Given their period range and spatial scales, these variations can be used to probe electrical conductivity within the asthenosphere and MTZ (Fig. 6). As was already discussed in Sect. 3.5, there were many works in the past decade which elaborated on space-time representation of the ionospheric sources, and inversion of daily band variations in terms of the mantle conductivity structure. Koch and Kuvshinov (2015) inverted Sq variations from the AWAGS array and derived a 3-D conductivity model of the mantle under the Australian continent. Notably both the source current and subsurface conductivity structures were reconstructed in an alternating way (see Sect. 3.7). Guzavina et al. (2019) developed this approach further and applied it to a global network of geomagnetic observatories to derive conductivity profiles under their locations. There, authors used the concept of local-to-global TFs as defined in Eqs. (32)–(33) in order to work with spatially complex Sq source currents. Zhang et al. (2022) used an alternating approach and a physics-based spatial basis to describe the ionospheric source currents (see Sect. 3.5) and inverted daily band magnetic field variations for the global average conductivity of the asthenosphere and MTZ. All studies interpreted the resulting conductivity models in terms of the mantle water content or possible partial melting. Although the described works illustrate a remarkable progress within the last decade,

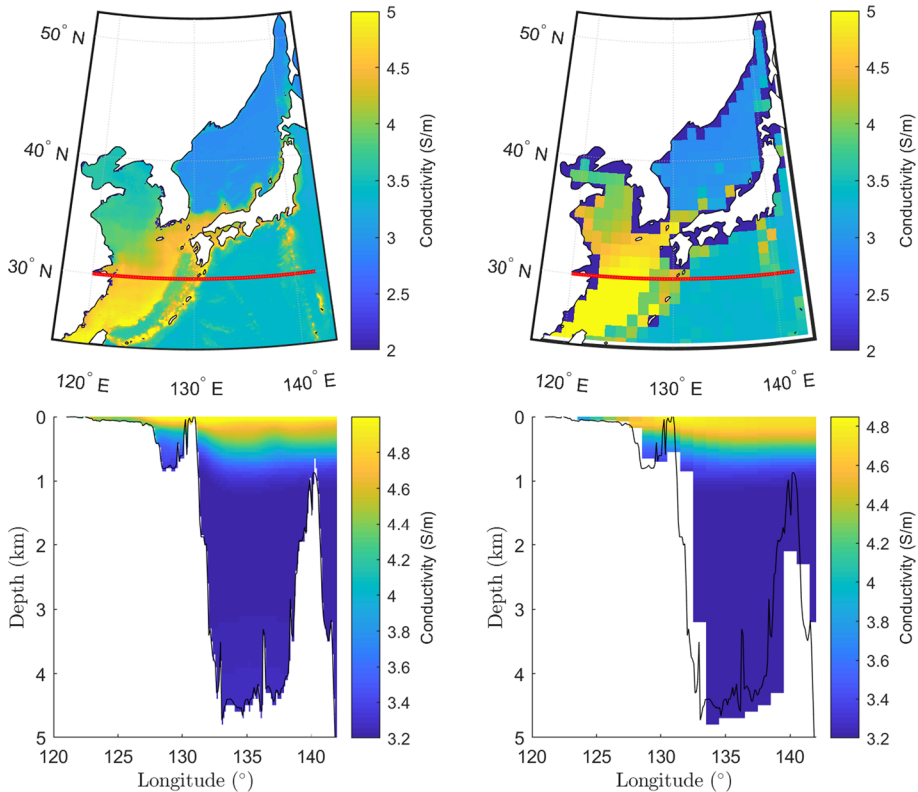


Fig. 12 Depth-averaged (top) and, for the cross-section in red, depth-dependent (bottom) electrical conductivity of the west Pacific coast. Left and right figures were derived from Grayver (2021) and Tyler et al. (2017), respectively

they all were limited to using ground data from global observatories or large-scale arrays. The extension of these methods to satellite data could be a major step forward. However, the challenge of using daily band variations with satellite data is twofold: (i) unlike for the long-period magnetospheric sources, the major part of the signal in the daily band is generated in regions below the LEO satellites (e.g. E-region at $\approx 90 - 130$ km altitude), rendering both inducing and induced parts of the field to be of the internal origin, and (ii) LEO satellites occasionally pass through current-generating regions where the magnetic field is not potential (Sabaka et al. 2010). These complications invalidate most of the developed approaches that target ground magnetic data processing and modelling. Importantly, a new generation of methods presented by Zhang et al. (2022); Zenhäusern et al. (2021) together with the inversion approach of Min and Grayver (2023) can in principle be extended to also work with satellite data, but this extension requires further developments.

4.4 Long-Period Band

A new generation of global 3-D conductivity models based on long-period EM responses was presented by different groups. Semenov and Kuvshinov (2012), Sun et al. (2015), Li

et al. (2020) used GDS (that is, C_1) responses to derive global 3-D conductivity models of the MTZ and upper parts of the lower mantle. Note that the method presented by Sun et al. (2015) also implements an advanced treatment of the ionospheric currents, which are known to bias conductivity models in conventional approaches where the sources is assumed to be described by the first zonal SH function (P_1^0 assumption). Püthe et al. (2015b), Grayver et al. (2021) also presented an approach that allows one to handle complex external sources and reconstruct the 3-D conductivity from the ground observatory and satellite data. These ideas were further developed by Min and Grayver (2023) who developed the simultaneous inversion for the inducing source and subsurface conductivity whereby the physical link between the inducing source and the subsurface conductivity is explicitly enforced. These methods allow one to mitigate many limitations imposed by the conventional Gauss-based workflow or Z/H method, which nonetheless are still widely applied, despite their well-known and documented limitations (see Sect. 3.5).

Kuvshinov et al. (2021), Velínský and Knopp (2021) presented first 3-D conductivity models produced with the use of satellite data. In these studies, data from the ESA Swarm and CryoSat-2 platform magnetometer were used along with the ground observatories. The inducing and induced time series of SH coefficients up to degree and order three were either fitted directly in time domain or transformed to the frequency domain for estimation of the Q -matrix TFs (see Sect. 3.3). Note the focus was on fitting the long period (> 1 day) variations of the predominantly magnetospheric origin, hence these models have rather limited sensitivity to the mantle structure above the MTZ. Additionally, a degree 3 SH representation of the induced fields means that the final models have a low spatial resolution, hence many geological phenomena that can potentially have a significant signature in lateral conductivity gradients still remain unresolved.

In addition to the global 3-D models, Koyama et al. (2014), Shimizu et al. (2010) inverted GDS responses for 3-D conductivity distribution under Australia and/or Pacific regions. Zhang and Yang (2022) presented a 3-D resolution study and concluded that if measurements are sufficiently dense, conductivity anomalies due to stagnant slabs can be detected by GDS responses, assuming that there are no source effects which would distort the C_1 responses. Several studies inverted GDS responses for local 1-D conductivity profiles (Munch et al. 2018; Zhang et al. 2021; Yuan et al. 2020; Zhang et al. 2020). A number of studies derived global average conductivity profiles by inverting the global average transfer function (Püthe et al. 2015a; Yao et al. 2023a; Grayver et al. 2017; Verhoeven et al. 2021; Velínský and Knopp 2021; Constable et al. 2022).

The aforementioned works mainly concentrate on the conductivity structure down to depths of ≈ 1600 km, thus a large part of the lower mantle is not considered/resolved. As of today, electrical structure of the lower mantle remains poorly constrained and understood. Figure 6 shows that in order to reach depths of ≥ 1000 km, variations from global sources (SH degrees 1–2) with periods ≈ 30 days are needed. Therefore, usage of long calibrated ground and satellite time series should enable new constraints on the conductivity structure of the lower mantle. In theory, the limit of no induction (i.e. the depth at which geometric attenuation dominates over EM induction) is within the core for the largest possible spatial source (Fig. 6). Thus, conductivity structure at the core–mantle boundary (CMB) affects EM induction responses at very long periods (Velínský and Finlay 2011; Velínský et al. 2012; Constable et al. 2022). In reality, reaching these depths requires a sufficiently powerful external source at relevant periods (Olsen 2007; Constable 2016). One possibility is to use natural variations induced at the solar cycle period (Olsen 1999b; Constable et al. 2022) and sub-harmonics that would allow us to reach depths of 2500–2700 km (Fig. 6). However, reliable estimation of EM responses at these periods requires high quality

multi-decadal time series and a tailored pre-processing in order to minimize the effect due to core field variations. Sufficiently long time series are presently available only for a few ground observatories (Fig. 2), although the problem will render feasible with time as the era of high-quality modern ground and satellite magnetic observations continues.

An interesting avenue for future research, which also partially mitigates the loss of sensitivity of EM induction responses towards the lowermost mantle, is to constrain the lower mantle conductivity by using both the top-down sounding approach and the bottom-up mechanisms, namely the fast core field variations. In addition to the mechanical coupling at the CMB, core is also electromagnetically coupled to the lower mantle and magnetic field variations at relevant periods offer a way to impose constraints on the conductivity of the lowermost mantle. Some recent references that document efforts in this direction include Pinheiro and Jackson (2008); Pinheiro et al. (2015) where the focus was on geomagnetic jerks, as well as works of Schaeffer and Jault (2016), Jault (2015), Gillet et al. (2017) where the conductance of the lowermost mantle was inferred from studying the interactions between MHD waves and the mantle at the CMB. It should be noted at this point that without injecting some prior knowledge and constraints into the problem, the magnetic field variations from the core and lower-mantle cannot be separated within the potential field representation.

4.5 Joint Inversions with Multiple Sources

Owing to differences in the source representation, data processing and modelling, most studies focus on variations from a single band, thus using only plane-wave, daily or long-period responses. Combination of EM variations across as wide a frequency range as possible will clearly be beneficial because it will allow us to constrain a much larger depth column. Figure 13 illustrates this idea showing inversion results for cases when EM transfer functions from different bands are inverted separately and jointly. Although the responses from different bands may not have overlapping periods, they have complementary sensitivities; hence, their joint inversion would take the full advantage of this property.

In the last decade, there were several studies which successfully combined responses from different sources and inverted them simultaneously for a single conductivity model. Matsuno et al. (2017) combined MT and GDS responses estimated from OBEM data collected in the Pacific East of Japan. Authors inverted data for 1-D conductivity of the upper mantle and MTZ to study potential presence of partially molten material. Chen et al. (2022) performed similar work by using data from a few islands and a concept of new TFs, which allowed them to work with more realistic sources. A stochastic inversion algorithm was used whereby the effect of the 3-D ocean was taken into account. Munch et al. (2020) inverted jointly daily band and magnetospheric responses using a stochastic optimization framework for a number of continental observatories and constrained the mantle water content for these locations using the thermodynamic phase equilibria modelling and laboratory conductivity measurements. Also there authors used new local-to-global transfer functions to accommodate a more realistic model of ionospheric and magnetospheric sources. In Zhang et al. (2023a), the authors also performed a joint inversion of the daily band ionospheric and long period magnetospheric signals to constrain the water content of the upper mantle and MTZ. A physics-based description of the ionospheric source was used (Egbert et al. 2020), while conventional C_1 responses were estimated at periods longer than one day. Yao et al. (2023b) implemented a 1-D Bayesian inversion of MT and C_1 responses. Grayver et al. (2017), Kuvshinov et al. (2021) inverted long-period

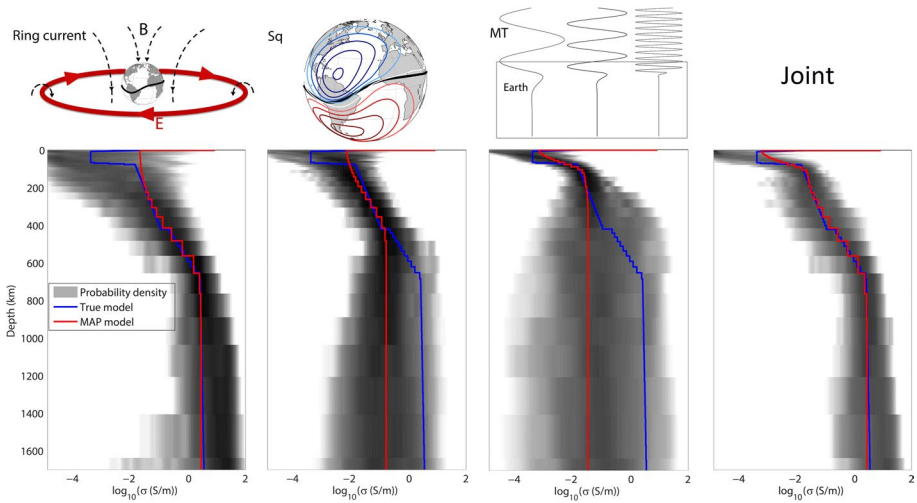


Fig. 13 Synthetic probabilistic inversion of EM responses using different spectral bands separately and jointly (rightmost plot). Transfer functions from different period bands are defined as: periods 2–180 days are long-period responses due to a source described by the first zonal harmonic, 4–24 h are daily band Sq variations, and 1–12000 s is the plane-wave MT band. MAP (red lines) denotes the Maximum A posteriori Probability models

global magnetospheric responses and ocean tidal magnetic signals jointly to reconstruct the average global conductivity profile. Note in these models the upper mantle is mostly constrained only below the oceans, because tidal magnetic signals are effectively zero over the land areas. These models were used for geomagnetic field modelling (Finlay et al. 2020) or as a starting model for 3-D EM inversion of the USArray (Munch and Grayver 2023) or global Q-matrix transfer functions (Kuvshinov et al. 2021).

Note that all aforementioned studies used 1-D conductivity parameterizations of the mantle (that is, inverting either for local or global/regional average radial conductivity profiles). Extensions to 3-D imaging with multiple sources from different spectral bands is an active area of research.

5 Extraterrestrial Studies

Since measuring EM induction effects can be done without a physical coupling, any magnetometer measurement of the full vector field around an electrically conductive body is a candidate for EM induction sounding. Similar to the Earth, the major challenge lies in an ability to quantitatively characterize the inducing source and separate the inducing and induced components. Unlike Earth, however, we know much less about electromagnetic environments around other planets, although this situation is changing as new missions equipped with magnetometers are in construction, cruising or already in orbit around other bodies. Therefore, while methods and modelling tools developed for Earth are in principle useful for planetary studies, they are not always directly applicable for other bodies in the solar system because of the existing and still sparsely sampled specifics of surrounding magnetic field environments that dominate observations. A comprehensive review of

the induced magnetic fields around other bodies in the solar system is given in Saur et al. (2010), and the reader is referred to this work for more details and description of methods. The rest of this section is a short overview of works published after 2010.

Discovery of the subsurface ocean on the Jovian moon Europa (Neubauer 1998; Khurana et al. 1998; Kivelson et al. 2000) is a prime example of a case where EM induction has played the major role. There, the currents in the moon are induced due to the orbital motion through the varying external magnetic field of the host (Jupiter in this case). The main excitation in this case occurs at the synodic period (and sub-harmonics), although measurable response at other periods also exist (e.g. Seufert et al. 2011) and will be constrained by new missions. Since the pioneering work in the 1990s, the EM induction in the Jovian moons has been thoroughly explored and documented (Seufert et al. 2011; Biersteker et al. 2022; Liuzzo et al. 2018; Hartkorn and Saur 2017; Vance et al. 2021). Signals induced in the subsurface of some Galilean satellites can also alter the observed aurora signatures, allowing an indirect inference of the interior electrical conductivity (Saur et al. 2015). So far, mostly observations from the Galileo mission flybys were used to study attenuation of the magnetic field due to putative subsurface oceans. However, new measurements by the Juno spacecraft already enable new models (Weber et al. 2022; Duling et al. 2022) and together with the launched JUICE (Grasset et al. 2013) and planned Europa Clipper (Kivelson et al. 2023) missions will unlock a whole new set of opportunities in this field, including measuring an amplitude and phase shift at multiple periods, which will permit better constraints on the conductivity and thickness of the subsurface layers. Further, multiple studies have simulated EM induction responses for bodies with hypothesized subsurface fluid reservoirs, including Ceres (Grimm et al. 2021a), moons of Uranus (Cochrane et al. 2021; Weiss et al. 2021; Arridge and Eggington 2021) and Neptune (Saur et al. 2010; Cochrane et al. 2022). Finally, dedicated MT instruments for a lander mission were also developed (Grimm et al. 2021b) and may become a part of the scientific payload in future missions to moons and planets.

The earliest application of the EM induction sounding beyond the Earth was during the Apollo era. Namely, simultaneous observations of the magnetic field from the Apollo 12 lander and the Explorer 35 orbiter were used to derive a broadband EM transfer function and invert it for a lunar conductivity profile (Dyal and Parkin 1973; Sonett 1975). A recent integrated analysis and interpretation of the Apollo 12 and Explorer 35 transfer functions were presented by Grimm (2013, 2023). However, the original calibrated magnetic field time series from Apollo magnetometers are seemingly lost or at least cannot be easily retrieved in the public domain, hence a full reprocessing using modern tools is not presently possible. Since the Apollo era, Lunar Prospector and Kaguya Selene spacecrafts collected vector magnetic field data while on low orbits around Moon. These data were used by Shimizu et al. (2013) to place an upper bound on the lunar core size and more recently by Mittelholz et al. (2021) to derive a global average TF (Sect. 3.3) and invert it in terms of lunar mid-mantle conductivity. Independently, Fuqua Haviland et al. (2019), Grimm (2013) simulated a plasma environment around Moon to better quantify the contributions from plasma and induced fields. A future lander (Grimm and Delory 2012; Haviland et al. 2022) and reprocessing of the legacy Apollo magnetic data (provided it can be recovered and calibrated) will unlock new insights into lunar interior.

Another extraterrestrial body for which induction studies were ample in the last decade is Mercury. This was largely enabled through the analysis of magnetic measurements taken by the MESSENGER spacecraft. Unfortunately, a very elliptic orbit of the spacecraft with

the perigee close to the north pole imposed rather strong constraints on its usability for the induction studies. Nevertheless, the MESSENGER data were used by researchers to determine the core size and place some bounds on the total conductance of its mantle (Johnson et al. 2016; Wardinski et al. 2019; Shimizu et al. 2021). The potential field assumption adopted in all of these studies was discussed and validated by Toepfer et al. (2021). The ESA BepiColombo mission, a constellation of two magnetometer-carrying spacecrafts (Heyner et al. 2021), is planned to enter its nominal orbital configuration near Mercury in late 2025. One of the spacecraft will be inserted into a circular polar orbit, offering a favourable configuration for the induction studies (Zomerdijsk-Russell et al. 2021, 2023).

Electromagnetic interactions for exoplanetary systems have also received a lot of attention in recent years. Main effects of EM star–planet interactions include energy channeling, atmospheric escape, orbit migration and interior heating (Strugarek 2017). In view of this, an ability to model electromagnetic induction within exoplanets in consistency with other exterior/interior models is an important ingredient for simulating their long-term evolution and assessing habitability. Most exoplanetary systems are constructed as solar system analogues; therefore, our knowledge about electrical structure of bodies in the solar system as well as our ability to model EM induction effects within them has direct uses in the field of exoplanets. For instance, interior heating of rocky exoplanets has been simulated for periodic (Kislyakova et al. 2017; Kelbert et al. 2019a; Noack et al. 2021; Chyba et al. 2021; Kislyakova et al. 2023) excitation (specifically, motion of planets through a varying magnetic field of the hosting body) and transient events such as Interplanetary Coronal Mass Ejections (ICMEs) (Grayver et al. 2022) where the EM induction heating (through Ohmic dissipation) was found to be potentially very significant. Similar analysis was done by Bromley and Kenyon (2019) for asteroids and small planetesimals. The role of EM interactions in orbital dynamics of rocky bodies was further studied in Bromley and Kenyon (2022), Kotera et al. (2016).

6 Conclusions

I am confident that the field of large-scale electromagnetic induction and imaging has a bright future ahead with many opportunities to be taken advantage of. Given how little we know about deep electrical structure of our planet (let alone other planets and moons), this field holds a large potential for generating “disruptive” science in the coming decades (Park et al. 2023). A lot of questions pertinent to the thermo-chemical structure of the mantle, formation of mineral and geothermal systems, modelling of space weather hazards and nature of core–mantle coupling will benefit enormously from quality electrical conductivity models and/or modern EM modelling tools. This need will drive the field forward and working with adjacent disciplines offers ample opportunities for an exciting inter-disciplinary research. However, similar to many contemporary problems in science, maintaining strong engagement with other fields of Earth sciences will be required (Okamura 2019).

Another set of opportunities lies in planetary/space sciences, where the treatment of induction (if any at all) exists only at a rudimentary level. Magnetic field observations from new missions (to be) launched to planets and moons will present a new set of opportunities and challenges for planetary sciences. Beyond our solar system, potential observations and modelling of electromagnetic star–planet interactions have become an independent niche in the exoplanetary community. There is a high demand in expertise and knowledge collected

within our Earth-focused community, although it requires adaptation to serve the needs of the planetary sciences community. Those who are ready to look across the boundaries of their immediate research field and talk to these communities will benefit enormously.

I hope that personal reflections and thoughts found in this review were expressed in a well-justified and reasoned way. Although I strove for completeness, I shall apologize in case a reader did not find anticipated references in this work.

Acknowledgements This work was supported by the Heisenberg Grant from the German Research Foundation, Deutsche Forschungsgemeinschaft (Project No. 465486300) and ESA Swarm DISC project No. 4000109587. I am indebted to many excellent colleagues for insightful discussions and collaborations on the topic of this review throughout the years. I thank two reviewers and the editor Dr. Anne Neska for their constructive comments that helped improve the manuscript.

Funding Open Access funding enabled and organized by Projekt DEAL.

Declarations

Conflict of interest I declare no conflicts of interest associated with this work.

Open Access This article is licensed under a Creative Commons Attribution 4.0 International License, which permits use, sharing, adaptation, distribution and reproduction in any medium or format, as long as you give appropriate credit to the original author(s) and the source, provide a link to the Creative Commons licence, and indicate if changes were made. The images or other third party material in this article are included in the article's Creative Commons licence, unless indicated otherwise in a credit line to the material. If material is not included in the article's Creative Commons licence and your intended use is not permitted by statutory regulation or exceeds the permitted use, you will need to obtain permission directly from the copyright holder. To view a copy of this licence, visit <http://creativecommons.org/licenses/by/4.0/>.

References

- Alken P, Olsen N, Finlay CC (2020) Co-estimation of geomagnetic field and in-orbit fluxgate magnetometer calibration parameters. *Earth Planets Space* 72:1–32. <https://doi.org/10.1186/s40623-020-01163-9>
- Alken P, Thébault E, Beggan CD et al (2021) International geomagnetic reference field: the thirteenth generation. *Earth Planets Space* 73(1):49. <https://doi.org/10.1186/s40623-020-01288-x>
- Anderson BJ, Angappan R, Barik A et al (2021) Iridium communications satellite constellation data for study of Earth's magnetic field. *Geochem Geophys Geosyst* 22(8):e2020GC009,515. <https://doi.org/10.1002/essoar.10506892.1>
- Anderssen R (1975) On the inversion of global electromagnetic induction data. *Phys Earth Planet Inter* 10(3):292–298. [https://doi.org/10.1016/0031-9201\(75\)90055-2](https://doi.org/10.1016/0031-9201(75)90055-2)
- Araya Vargas J, Ritter O (2016) Source effects in mid-latitude geomagnetic transfer functions. *Geophys J Int* 204(1):606–630. <https://doi.org/10.1093/gji/ggv474>
- Arridge CS, Eggington JW (2021) Electromagnetic induction in the icy satellites of Uranus. *Icarus* 367(114):562. <https://doi.org/10.1016/j.icarus.2021.114562>
- Autio U, Smirnov MY (2020) Magnetotelluric array in the central Finnish Lapland I: extreme data characteristics. *Tectonophysics* 794(228):613. <https://doi.org/10.1016/j.tecto.2020.228613>
- Bailey R (1973) Global geomagnetic sounding-methods and results. *Phys Earth Planet Inter* 7(3):234–244. [https://doi.org/10.1016/0031-9201\(73\)90050-2](https://doi.org/10.1016/0031-9201(73)90050-2)
- Baltazar-Soares P, Martínez-Moreno F, Alves Ribeiro J et al (2023) Crustal imaging of Portugal mainland using magnetotelluric data. *Earth Space Sci* 10(7):e2022EA002,732. <https://doi.org/10.1029/2022ea002732>
- Bangertner W, Rannacher R (2003) Adaptive finite element methods for differential equations. Springer Science & Business Media, Berlin. <https://doi.org/10.1007/978-3-0348-7605-6>
- Banks R (1969) Geomagnetic variations and the electrical conductivity of the upper mantle. *Geophys J Int* 17(5):457–487. <https://doi.org/10.1111/j.1365-246x.1969.tb00252.x>

- Baumjohann W, Blanc M, Fedorov A et al (2010) Current systems in planetary magnetospheres and ionospheres. *Space Sci Rev* 152:99–134. https://doi.org/10.1007/978-1-4419-5901-0_4
- Berdichevsky MN, Dmitriev VI (2002) Magnetotellurics in the context of the theory of ill-posed problems. *Soc Explor Geophys* doi 10(1190/1):9781560802068
- Biersteker JB, Weiss BP, Cochrane CJ, et al (2022) Revealing the interior structure of icy moons with a Bayesian approach to magnetic induction measurements. <https://doi.org/10.3847/psj/acc331>
- Bromley BC, Kenyon SJ (2019) Ohmic heating of asteroids around magnetic stars. *Astrophys J* 876(1):17. <https://doi.org/10.3847/1538-4357/ab12e9>
- Bromley BC, Kenyon SJ (2022) Magnetic interactions in orbital dynamics. *Astron J* 164(6):229. <https://doi.org/10.3847/1538-3881/ac9301>
- Chamalaun F, Barton C (1990) Comprehensive mapping of Australia's geomagnetic variations. <https://doi.org/10.1029/90eo00376>
- Chapman S (1919) I. The solar and lunar diurnal variations of terrestrial magnetism. *Philos Trans R Soc Lond Ser A Contain Pap Math Phys Charact* 218(561–569):1–118. <https://doi.org/10.1098/rsta.1919.0001>
- Chen C, Kruglyakov M, Kuvshinov A (2020) a new method for accurate and efficient modeling of the local ocean induction effects. Application to long-period responses from island geomagnetic observatories. *Geophys Res Lett* 47(8):e2019GL086,351. <https://doi.org/10.1002/essoar.10502153.1>
- Chen C, Kuvshinov A, Kruglyakov M et al (2022) Constraining the crustal and mantle conductivity structures beneath islands by a joint inversion of multi-source magnetic transfer functions. *J Geophys Res Solid Earth*. <https://doi.org/10.1029/2022JB024106>
- Cherevatova M, Smirnov MY, Jones A et al (2015) Magnetotelluric array data analysis from north-west Fennoscandia. *Tectonophysics* 653:1–19. <https://doi.org/10.1016/j.tecto.2014.12.023>
- Chulliat A, Vigneron P, Hulot G (2016) First results from the Swarm dedicated ionospheric field inversion chain. *Earth Planets Space* 68(1):1–18. <https://doi.org/10.1186/s40623-016-0481-6>
- Chyba CF, Hand KP, Thomas PJ (2021) Magnetic induction heating of planetary satellites: analytical formulae and applications. *Icarus* 360(114):360. <https://doi.org/10.1016/j.icarus.2021.114360>
- Cochrane C, Vance S, Nordheim T et al (2021) In search of subsurface oceans within the Uranian moons. *J Geophys Res Planets* 126(12):e2021JE006,956. <https://doi.org/10.1029/2021je006956>
- Cochrane C, Persinger R, Vance S et al (2022) Single-and multi-pass magnetometric subsurface ocean detection and characterization in icy worlds using principal component analysis (PCA): application to triton. *Earth Space Sci* 9(2):e2021EA002,034. <https://doi.org/10.1029/2021ea002034>
- Constable C (2016) Earth's electromagnetic environment. *Surv Geophys* 37(1):27–45. <https://doi.org/10.1007/s10712-015-9351-1>
- Constable C, Constable S (2023) A grand spectrum of the geomagnetic field. *Phys Earth Planet Inter*. <https://doi.org/10.1016/j.pepi.2023.107090>
- Constable S, Constable C, Korte M, et al (2022) A global EM induction response to 11 year period and the conductivity of the lower mantle. *Geochem Geophys Geosyst* 5(1)
- Dong SW, Li TD, Lü QT et al (2013) Progress in deep lithospheric exploration of the continental China: a review of the SinoProbe. *Tectonophysics* 606:1–13. <https://doi.org/10.1016/j.tecto.2013.05.038>
- Duan J, Kyi D, Jiang W (2020) AusLAMP: imaging the Australian lithosphere for resource potential, an example from northern Australia. In: AGU fall meeting abstracts, pp GP006–04, <https://doi.org/10.11636/134997>
- Duling S, Saur J, Clark G et al (2022) Ganymede MHD model: magnetospheric context for Juno's PJ34 flyby. *Geophys Res Lett* 49(24):e2022GL101,688. <https://doi.org/10.1029/2022gl101688>
- Dyal P, Parkin CW (1973) Global electromagnetic induction in the moon and planets. *Phys Earth Planet Inter* 7(3):251–265. [https://doi.org/10.1016/0031-9201\(73\)90052-6](https://doi.org/10.1016/0031-9201(73)90052-6)
- Egbert GD, Kelbert A (2012) Computational recipes for electromagnetic inverse problems. *Geophys J Int* 189(1):251–267. <https://doi.org/10.1111/j.1365-246x.2011.05347.x>
- Egbert GD, Alken P, Maute A et al (2020) Modeling diurnal variation magnetic fields for mantle induction studies. *Geophys J Int*. <https://doi.org/10.1093/gji/ggaa533>
- Ernst T, Nowożyński K, Jóźwiak W (2020) The reduction of source effect for reliable estimation of geomagnetic transfer functions. *Geophys J Int* 221(1):415–430. <https://doi.org/10.1093/gji/ggaa017>
- Everett ME, Chave AD (2019) On the physical principles underlying electromagnetic induction EM induction physical principles. *Geophysics* 84(5):W21–W32. <https://doi.org/10.1190/geo2018-0232.1>
- Fichtner A, Zunino A, Gebraad L et al (2021) Autotuning Hamiltonian Monte Carlo for efficient generalized nullspace exploration. *Geophys J Int* 227(2):941–968. <https://doi.org/10.1093/gji/ggab270>
- Finlay C, Lesur V, Thébault E et al (2017) Challenges handling magnetospheric and ionospheric signals in internal geomagnetic field modelling. *Space Sci Rev* 206:157–189. https://doi.org/10.1007/978-94-024-1225-3_7

- Finlay CC, Kloss C, Olsen N et al (2020) The CHAOS-7 geomagnetic field model and observed changes in the South Atlantic Anomaly. *Earth Planets Space* 72(1):1–31. <https://doi.org/10.1186/s40623-020-01252-9>
- Fujii I, Ookawa T, Nagamachi S et al (2015) The characteristics of geoelectric fields at Kakioka, Kanoya, and Memambetsu inferred from voltage measurements during 2000 to 2011. *Earth Planets Space* 67:1–17. <https://doi.org/10.1186/s40623-015-0241-z>
- Fuqua Haviland H, Poppe AR, Fatemi S et al (2019) Time-dependent hybrid plasma simulations of lunar electromagnetic induction in the solar wind. *Geophys Res Lett* 46(8):4151–4160. <https://doi.org/10.1029/2018gl080523>
- Ganushkina NY, Liemohn M, Dubyagin S (2018) Current systems in the Earth's magnetosphere. *Rev Geophys* 56(2):309–332. <https://doi.org/10.1002/2017rg000590>
- Gauss CF (1877) *Allgemeine Theorie des Erdmagnetismus*. Werke. Springer, Berlin, pp 119–193. https://doi.org/10.1007/978-3-642-49319-5_5
- Gillet N, Jault D, Canet E (2017) Excitation of travelling torsional normal modes in an Earth's core model. *Geophys J Int* 210(3):1503–1516. <https://doi.org/10.1093/gji/ggx237>
- Gjerloev J (2012) The SuperMAG data processing technique. *J Geophys Res Space Phys*. <https://doi.org/10.1029/2012ja017683>
- Grasset O, Dougherty M, Coustenis A et al (2013) JUPITER ICy moons Explorer (JUICE): an ESA mission to orbit Ganymede and to characterise the Jupiter system. *Planet Space Sci* 78:1–21. <https://doi.org/10.1016/j.pss.2012.12.002>
- Grayver A, Bower DJ, Saur J et al (2022) Interior heating of rocky exoplanets from stellar flares with application to TRAPPIST-1. *Astrophys J Lett* 941(1):L7. <https://doi.org/10.3847/2041-8213/aca287>
- Grayver AV (2021) Global 3-D electrical conductivity model of the world ocean and marine sediments. *Geochem Geophys Geosyst* 22(9):e2021GC009,950. <https://doi.org/10.1029/2021gc009950>
- Grayver AV, Olsen N (2019) The magnetic signatures of the M2, N2, and O1 oceanic tides observed in Swarm and CHAMP satellite magnetic data. *Geophys Res Lett* 46(8):4230–4238. <https://doi.org/10.1029/2019GL082400>
- Grayver AV, Schnepf NR, Kuvshinov AV et al (2016) Satellite tidal magnetic signals constrain oceanic lithosphere-asthenosphere boundary. *Sci Adv* 2(9):e1600,798. <https://doi.org/10.1126/sciadv.1600798>
- Grayver AV, Munch FD, Kuvshinov AV et al (2017) Joint inversion of satellite-detected tidal and magnetospheric signals constrains electrical conductivity and water content of the upper mantle and transition zone. *Geophys Res Lett* 44(12):6074–6081. <https://doi.org/10.1002/2017gl073446>
- Grayver AV, van Driel M, Kuvshinov AV (2019) Three-dimensional magnetotelluric modelling in spherical Earth. *Geophys J Int* 217(1):532–557. <https://doi.org/10.1093/gji/ggz030>
- Grayver AV, Kuvshinov A, Werthmüller D (2021) Time-domain modeling of three-dimensional earth's and planetary electromagnetic induction effect in ground and satellite observations. *J Geophys Res Space Phys* 126(3):e2020JA028,672. <https://doi.org/10.1029/2020ja028672>
- Griffiths DJ (2017) *Introduction to electrodynamics*. Cambridge University Press, Cambridge
- Grimm R, Castillo-Rogez J, Raymond C et al (2021) Feasibility of characterizing subsurface brines on Ceres by electromagnetic sounding. *Icarus* 362(114):424. <https://doi.org/10.1016/j.icarus.2021.114424>
- Grimm R, Nguyen T, Persyn S et al (2021) A magnetotelluric instrument for probing the interiors of Europa and other worlds. *Adv Space Res* 68(4):2022–2037. <https://doi.org/10.1016/j.asr.2021.04.011>
- Grimm RE (2013) Geophysical constraints on the lunar Procellarum KREEP Terrane. *J Geophys Res Planets* 118(4):768–778. <https://doi.org/10.1029/2012je004114>
- Grimm RE (2023) Lunar mantle structure and composition inferred from Apollo 12 - Explorer 35 electromagnetic sounding. *Icarus* p 115775. <https://doi.org/10.1016/j.icarus.2023.115775>,
- Grimm RE, Delory GT (2012) Next-generation electromagnetic sounding of the Moon. *Adv Space Res* 50(12):1687–1701. <https://doi.org/10.1016/j.asr.2011.12.014>
- Guzavina M, Grayver A, Kuvshinov A (2018) Do ocean tidal signals influence recovery of solar quiet variations? *Earth Planets Space* 70:1–15. <https://doi.org/10.1186/s40623-017-0769-1>
- Guzavina M, Grayver A, Kuvshinov A (2019) Probing upper mantle electrical conductivity with daily magnetic variations using global-to-local transfer functions. *Geophys J Int* 219(3):2125–2147. <https://doi.org/10.1093/gji/ggz412>
- Han Q, Hu X (2023) Three-dimensional magnetotelluric modeling in spherical and cartesian coordinate systems: a comparative study. *Earth Planet Phys*. <https://doi.org/10.26464/epp2023048>
- Hartkorn O, Saur J (2017) Induction signals from Callisto's ionosphere and their implications on a possible subsurface ocean. *J Geophys Res Space Phys* 122(11):677. <https://doi.org/10.1002/2017jg0024269>
- Haviland HF, Weber RC, Neal CR et al (2022) The lunar geophysical network landing sites science rationale. *Planet Sci J* 3(2):40. <https://doi.org/10.3847/psj/ac0f82>

- Heyner D, Auster HU, Fornaçon KH et al (2021) The BepiColombo planetary magnetometer MPO-MAG: what can we learn from the Hermean magnetic field? *Space Sci Rev* 217:1–71. <https://doi.org/10.1007/s11214-021-00822-x>
- Hobbs B (1975) Analytical solutions to global and local problems of electromagnetic induction in the earth. *Phys Earth Planet Inter* 10(3):250–261. [https://doi.org/10.1016/0031-9201\(75\)90051-5](https://doi.org/10.1016/0031-9201(75)90051-5)
- Huebert J, Eaton E, Beggan C (2022) Developing a UK new ground electric field model for SWIMMR N4 (SAGE): interim report URL <https://nora.nerc.ac.uk/id/eprint/533349>
- Hulot G, Leger JM, Clausen LBN, et al (2021) NanoMagSat, a 16U nanosatellite constellation high-precision magnetic project to monitor the Earth's magnetic field and ionospheric environment. In: EGU general assembly abstracts, <https://doi.org/10.5194/egusphere-egu21-14660>
- Hunt BJ (2005) *The maxwellians*. Cornell University Press, New York
- Jault D (2015) Illuminating the electrical conductivity of the lowermost mantle from below. *Geophys J Int* 202(1):482–496. <https://doi.org/10.1093/gji/ggv152>
- Johnson CL, Philpott LC, Anderson BJ et al (2016) MESSENGER observations of induced magnetic fields in Mercury's core. *Geophys Res Lett* 43(6):2436–2444. <https://doi.org/10.1002/2015gl067370>
- Jones AG, Spratt J (2002) A simple method for deriving the uniform field MT responses in auroral zones. *Earth Planets Space* 54(5):443–450. <https://doi.org/10.1186/BF03353035>
- Kelbert A (2020) The role of global/regional earth conductivity models in natural geomagnetic hazard mitigation. *Surv Geophys* 41(1):115–166. <https://doi.org/10.1007/s10712-019-09579-z>
- Kelbert A, Schultz A, Egbert G (2009) Global electromagnetic induction constraints on transition-zone water content variations. *Nature* 460(7258):1003–1006. <https://doi.org/10.1038/nature08257>
- Kelbert A, Kuvshinov A, Velímský J et al (2014) Global 3-D electromagnetic forward modelling: a benchmark study. *Geophys J Int* 197(2):785–814. <https://doi.org/10.1093/gji/ggu028>
- Kelbert A, Bedrosian PA, Murphy BS (2019a) The first 3D conductivity model of the contiguous United States: Reflections on geologic structure and application to induction hazards. *Geomagnetically induced currents from the Sun to the power grid*, pp 127–151. <https://doi.org/10.1002/9781119434412.ch8>
- Kelbert A, Erofeeva S, Trabant C et al (2019) Data sharing in magnetotellurics. *Eos Earth Space Sci News*. <https://doi.org/10.1029/2018EO112859>
- Khan A (2016) On Earth's mantle constitution and structure from joint analysis of geophysical and laboratory-based data: An example. *Surv Geophys* 37:149–189. <https://doi.org/10.1007/s10712-015-9353-z>
- Khurana K, Kivelson M, Stevenson D et al (1998) Induced magnetic fields as evidence for subsurface oceans in Europa and Callisto. *Nature* 395(6704):777–780. <https://doi.org/10.1038/27394>
- Kirkby A, Czarnota K, Huston DL et al (2022) Lithospheric conductors reveal source regions of convergent margin mineral systems. *Sci Rep* 12(1):8190. <https://doi.org/10.1038/s41598-022-11921-2>
- Kislyakova K, Noack L, Johnstone C et al (2017) Magma oceans and enhanced volcanism on TRAP-PIST-1 planets due to induction heating. *Nature Astron* 1(12):878–885. <https://doi.org/10.1038/s41550-017-0284-0>
- Kislyakova K, Noack L, Sanchis E et al (2023) Induction heating of planetary interiors in white dwarf systems. *Astron Astrophys*. <https://doi.org/10.1051/0004-6361/202245225>
- Kivelson MG, Khurana KK, Russell CT et al (2000) Galileo magnetometer measurements: a stronger case for a subsurface ocean at Europa. *Science* 289(5483):1340–1343. <https://doi.org/10.1126/science.289.5483.1340>
- Kivelson MG, Jia X, Lee KA et al (2023) The Europa Clipper Magnetometer. *Space Sci Rev* 219(6):48. <https://doi.org/10.1007/s11214-023-00989-5>
- Koch S, Kuvshinov A (2013) Global 3-D EM inversion of Sq variations based on simultaneous source and conductivity determination: concept validation and resolution studies. *Geophys J Int* 195(1):98–116. <https://doi.org/10.1093/gji/ggt227>
- Koch S, Kuvshinov A (2015) 3-D EM inversion of ground based geomagnetic Sq data. Results from the analysis of Australian array (AWAGS) data. *Geophys J Int* 200(3):1284–1296. <https://doi.org/10.1093/gji/ggu474>
- Korja T, Engels M, Zhamaletdinov AA et al (2002) Crustal conductivity in Fennoscandia—a compilation of a database on crustal conductance in the Fennoscandian Shield. *Earth Planets Space* 54(5):535–558. <https://doi.org/10.1186/bf03353044>
- Kotera K, Mottez F, Voisin G et al (2016) Do asteroids evaporate near pulsars? Induction heating by pulsar waves revisited. *Astron Astrophys* 592:A52. <https://doi.org/10.1051/0004-6361/201628116>
- Koyama T, Khan A, Kuvshinov A (2014) Three-dimensional electrical conductivity structure beneath Australia from inversion of geomagnetic observatory data: evidence for lateral variations in transition-zone temperature, water content and melt. *Geophys J Int* 196(3):1330–1350. <https://doi.org/10.1093/gji/ggt455>

- Kruglyakov M, Kuvshinov A (2022) Modelling tippers on a sphere. *Geophys J Int* 231(2):737–748. <https://doi.org/10.1093/gji/ggac199>
- Kruglyakov M, Kuvshinov A, Nair M (2022) A proper use of the adjacent land-based observatory magnetic field data to account for the geomagnetic disturbances during offshore directional drilling. *Space Weather* 20(12):e2022SW003,238. <https://doi.org/10.1029/2022SW003238>
- Kuvshinov A (2012) Deep electromagnetic studies from land, sea, and space: progress status in the past 10 years. *Surv Geophys* 33:169–209. <https://doi.org/10.1007/s10712-011-9118-2>
- Kuvshinov A, Semenov A (2012) Global 3-D imaging of mantle electrical conductivity based on inversion of observatory C-responses-I. An approach and its verification. *Geophys J Int* 189(3):1335–1352. <https://doi.org/10.1111/j.1365-246x.2011.05349.x>
- Kuvshinov A, Grayver A, Tøffner-Clausen L et al (2021) Probing 3-D electrical conductivity of the mantle using 6 years of Swarm, CryoSat-2 and observatory magnetic data and exploiting matrix Q-responses approach. *Earth Planets Space* 73(1):1–26. <https://doi.org/10.1186/s40623-020-01341-9>
- Lamb H (1883) XIII. On electrical motions in a spherical conductor. *Philos Trans R Soc Lond* 174:519–549. <https://doi.org/10.1098/rstl.1883.0013>
- Larsson J (2007) Electromagnetics from a quasistatic perspective. *Am J Phys* 75(3):230–239. <https://doi.org/10.1119/1.2397095>
- Laundal KM, Richmond AD (2017) Magnetic coordinate systems. *Space Sci Rev* 206(1–4):27–59. https://doi.org/10.1007/978-94-024-1225-3_3
- Laundal KM, Yee JH, Merkin VG et al (2021) Electrojet estimates from mesospheric magnetic field measurements. *J Geophys Res Space Phys* 126(5):e2020JA028,644. <https://doi.org/10.1029/2020JA028644>
- Li S, Weng A, Zhang Y et al (2020) Evidence of Bermuda hot and wet upwelling from novel three-dimensional global mantle electrical conductivity image. *Geochem Geophys Geosyst* 21(6):e2020GC009,016. <https://doi.org/10.1029/2020gc009016>
- Liuzzo L, Simon S, Feyerabend M (2018) Observability of Callisto's inductive signature during the JUPITER ICy moons Explorer mission. *J Geophys Res Space Phys* 123(11):9045–9054. <https://doi.org/10.1029/2018ja025951>
- Love JJ, Chulliat A (2013) An international network of magnetic observatories. *EOS Trans Am Geophys Union* 94(42):373–374. <https://doi.org/10.1002/2013eo420001>
- Lühr H, Maus S, Rother M et al (2002) First in-situ observation of night-time F region currents with the CHAMP satellite. *Geophys Res Lett* 29(10):127–1. <https://doi.org/10.1029/2001gl013845>
- Macmillan S, Olsen N (2013) Observatory data and the Swarm mission. *Earth Planets Space* 65(11):1355–1362. <https://doi.org/10.5047/eps.2013.07.011>
- Maksimov M, Velímský J (2017) Fast calculations of the gradient and the Hessian in the time-domain global electromagnetic induction inverse problem. *Geophys J Int* 210(1):270–283. <https://doi.org/10.1093/gji/ggx167>
- Martinec Z, Velímský J (2022) An electric circuit model of the Earth's polar electrojets and field-aligned currents for the estimation of magnetospheric magnetic field from along-track Swarm magnetic data. *Earth Planets Space* 74(1):157. <https://doi.org/10.1186/s40623-022-01716-0>
- Martinec Z, Velímský J, Haagmans R et al (2018) A two-step along-track spectral analysis for estimating the magnetic signals of magnetospheric ring current from Swarm data. *Geophys J Int* 212(2):1201–1217. <https://doi.org/10.1093/gji/ggx471>
- Martinec Z, Fullaer J, Velímský J et al (2021) A new integrated geophysical-petrological global 3-D model of upper-mantle electrical conductivity validated by the Swarm M2 tidal magnetic field. *Geophys J Int* 226(2):742–763. <https://doi.org/10.1093/gji/ggab130>
- Matsuno T, Suetsugu D, Baba K et al (2017) Mantle transition zone beneath a normal seafloor in the north-western Pacific: Electrical conductivity, seismic thickness, and water content. *Earth Planet Sci Lett* 462:189–198. <https://doi.org/10.1016/j.epsl.2016.12.045>
- Matsushita S (1975) Morphology of slowly-varying geomagnetic external fields-A review. *Phys Earth Planet Inter* 10(3):299–312. [https://doi.org/10.1016/0031-9201\(75\)90056-4](https://doi.org/10.1016/0031-9201(75)90056-4)
- Maxwell JC (1865) VIII. A dynamical theory of the electromagnetic field. *Philos Trans R Soc Lond* 155:459–512. <https://doi.org/10.1098/rstl.1865.0008>
- Min J, Grayver A (2023) Simultaneous inversion for source field and mantle electrical conductivity using the variable projection approach. *Earth, Planets and Space* 75(1):1–31. <https://doi.org/10.1186/s40623-023-01816-5>
- Minami T (2017) Motional induction by tsunamis and ocean tides: 10 years of progress. *Surv Geophys* 38:1097–1132. <https://doi.org/10.1007/s10712-017-9417-3>

- Mittelholz A, Grayver A, Khan A et al (2021) The global conductivity structure of the lunar upper and midmantle. *J Geophys Res Planets* 126(11):e2021JE006,980. <https://doi.org/10.1029/2021je006980>
- Munch FD, Grayver A (2023) Multi-scale imaging of 3-D electrical conductivity structure under the contiguous US constrains lateral variations in the upper mantle water content. *Earth Planet Sci Lett* 602(117):939. <https://doi.org/10.1016/j.epsl.2022.117939>
- Munch FD, Grayver A, Kuvshinov A et al (2018) Stochastic inversion of geomagnetic observatory data including rigorous treatment of the ocean induction effect with implications for transition zone water content and thermal structure. *J Geophys Res Solid Earth* 123(1):31–51. <https://doi.org/10.1002/2017jb014691>
- Munch FD, Grayver AV, Guzavina M et al (2020) Joint inversion of daily and long-period geomagnetic transfer functions reveals lateral variations in mantle water content. *Geophys Res Lett* 47(10):e2020GL087,222. <https://doi.org/10.1029/2020gl087222>
- Murphy BS, Egbert GD (2018) Source biases in midlatitude magnetotelluric transfer functions due to Pc3-4 geomagnetic pulsations. *Earth Planets Space* 70:1–9. <https://doi.org/10.1186/s40623-018-0781-0>
- Murphy BS, Lucas GM, Love JJ et al (2021) Magnetotelluric sampling and geoelectric hazard estimation: are national-scale surveys sufficient? *Space Weather* 19(7):e2020SW002,693. <https://doi.org/10.1029/2020sw002693>
- Murphy BS, Bedrosian PA, Kelbert A (2023) Geoelectric constraints on the Precambrian assembly and architecture of southern Laurentia. In: *Laurentia: Turning Points in the Evolution of a Continent*. Geological Society of America, [https://doi.org/10.1130/2022.1220\(13\)](https://doi.org/10.1130/2022.1220(13))
- Neska A, Reda JT, Neska ML et al (2018) On the relevance of source effects in geomagnetic pulsations for induction soundings. In: *Annales geophysicae, copernicus publications* Göttingen, Germany, pp 337–347. <https://doi.org/10.5194/angeo-36-337-2018>
- Neubauer FM (1998) The sub-Alfvénic interaction of the Galilean satellites with the Jovian magnetosphere. *J Geophys Res Planets* 103(E9):19843–19866. <https://doi.org/10.1029/97JE03370>
- Noack L, Kisyakova K, Johnstone C et al (2021) Interior heating and outgassing of Proxima Centauri b: identifying critical parameters. *Astron Astrophys* 651:A103. <https://doi.org/10.1051/0004-6361/202040176>
- Okamura K (2019) Interdisciplinarity revisited: evidence for research impact and dynamism. Palgrave Commun. <https://doi.org/10.1057/s41599-019-0352-4>
- Olsen N (1997) Ionospheric F region currents at middle and low latitudes estimated from Magsat data. *J Geophys Res Space Phys* 102(A3):4563–4576. <https://doi.org/10.1029/96JA02949>
- Olsen N (1999) Induction studies with satellite data. *Surv Geophys* 20(3–4):309–340. <https://doi.org/10.1023/A:1006611303582>
- Olsen N (1999) Long-period (30 days-1 year) electromagnetic sounding and the electrical conductivity of the lower mantle beneath Europe. *Geophys J Int* 138(1):179–187. <https://doi.org/10.1046/j.1365-246x.1999.00854.x>
- Olsen N (2007) Natural sources for electromagnetic induction studies. In: *Encyclopedia of geomagnetism and paleomagnetism*, pp 696–700. https://doi.org/10.1007/978-1-4020-4423-6_219
- Olsen N, Friis-Christensen E, Floberghagen R et al (2013) The Swarm satellite constellation application and research facility (SCARF) and Swarm data products. *Earth Planets Space* 65:1189–1200. <https://doi.org/10.5047/eps.2013.07.001>
- Olsen N, Albini G, Bouffard J et al (2020) Magnetic observations from CryoSat-2: calibration and processing of satellite platform magnetometer data. *Earth Planets Space* 72:1–18. <https://doi.org/10.1186/s40623-020-01171-9>
- Özaydın S, Selway K (2020) MATE: an analysis tool for the interpretation of magnetotelluric models of the mantle. *Geochem Geophys Geosyst* 21(9):e2020GC009,126. <https://doi.org/10.1029/2020gc009126>
- O’Leary DP, Rust BW (2013) Variable projection for nonlinear least squares problems. *Comput Optim Appl* 54:579–593. <https://doi.org/10.1007/s10589-012-9492-9>
- Pankratov O, Kuvshinov A (2015) General formalism for the efficient calculation of the Hessian matrix of EM data misfit and Hessian-vector products based upon adjoint sources approach. *Geophys J Int* 200(3):1449–1465. <https://doi.org/10.1093/gji/ggu476>
- Park M, Leahey E, Funk RJ (2023) Papers and patents are becoming less disruptive over time. *Nature* 613(7942):138–144. <https://doi.org/10.1038/s41586-022-05543-x>
- Parkinson W (1988) The global conductivity distribution. *Surv Geophys* 9(3–4):235–243. <https://doi.org/10.1007/bf01901624>
- Pinheiro K, Jackson A (2008) Can a 1-D mantle electrical conductivity model generate magnetic jerk differential time delays? *Geophys J Int* 173(3):781–792. <https://doi.org/10.1111/j.1365-246x.2008.03762.x>

- Pinheiro KJ, Jackson A, Amit H (2015) On the applicability of Backus' mantle filter theory. *Geophys J Int* 200(3):1336–1346. <https://doi.org/10.1093/gji/ggu477>
- Pommier A (2014) Interpretation of magnetotelluric results using laboratory measurements. *Surv Geophys* 35:41–84. <https://doi.org/10.1007/s10712-013-9226-2>
- Price AT (1973) The theory of geomagnetic induction. *Phys Earth Planet Int* 7(3):227–233. [https://doi.org/10.1016/0031-9201\(73\)90049-6](https://doi.org/10.1016/0031-9201(73)90049-6)
- Püthe C, Kuvshinov A (2014) Mapping 3-D mantle electrical conductivity from space: a new 3-D inversion scheme based on analysis of matrix Q-responses. *Geophys J Int* 197(2):768–784. <https://doi.org/10.1093/gji/ggu027>
- Püthe C, Kuvshinov A, Khan A et al (2015) A new model of Earth's radial conductivity structure derived from over 10 yr of satellite and observatory magnetic data. *Geophys Suppl Mon Notices R Astron Soc* 203(3):1864–1872. <https://doi.org/10.1093/gji/ggv407>
- Püthe C, Kuvshinov A, Olsen N (2015) Handling complex source structures in global EM induction studies: from C-responses to new arrays of transfer functions. *Geophys J Int* 201(1):318–328. <https://doi.org/10.1093/gji/ggv021>
- Qian L, Burns AG, Emery BA et al (2014) The NCAR TIE-GCM: A community model of the coupled thermosphere/ionosphere system. Modeling the ionosphere–thermosphere system, pp 73–83. <https://doi.org/10.1002/9781118704417.ch7>
- Reagan J, Zweng M, Seidov D et al (2019) WORLD OCEAN ATLAS 2018 Volume 6: Conductivity. UMBC joint center for earth systems technology URL <http://hdl.handle.net/11603/24723>
- Ren Z, Kalscheuer T (2020) Uncertainty and resolution analysis of 2D and 3D inversion models computed from geophysical electromagnetic data. *Surv Geophys* 41(1):47–112. <https://doi.org/10.1007/s10712-019-09567-3>
- Richmond A, Thayer J (2000) Ionospheric electrodynamics: a tutorial. *Magnetos Curr Syst* 118:131–146. <https://doi.org/10.1029/gm118p0131>
- Richmond AD (2017) Ionospheric electrodynamics. *Handbook of atmospheric electrodynamics* (1995). CRC Press, Boca Raton, pp 249–290. <https://doi.org/10.1029/GM118p0131>
- Rikitake T (1973) Global electrical conductivity of the earth. *Phys Earth Planet Inter* 7(3):245–250. [https://doi.org/10.1016/0031-9201\(73\)90051-4](https://doi.org/10.1016/0031-9201(73)90051-4)
- Roberts R (1986) Global electromagnetic induction. *Surv Geophys* 8(3):339–374. <https://doi.org/10.1007/bf01904064>
- Romano G, Balasco M, Lapenna V et al (2014) On the sensitivity of long-term magnetotelluric monitoring in Southern Italy and source-dependent robust single station transfer function variability. *Geophys J Int* 197(3):1425–1441. <https://doi.org/10.1093/gji/ggu083>
- Sabaka TJ, Olsen N, Langel RA (2002) A comprehensive model of the quiet-time, near-Earth magnetic field: phase 3. *Geophys J Int* 151(1):32–68. <https://doi.org/10.1046/j.1365-246x.2002.01774.x>
- Sabaka TJ, Hulot G, Olsen N (2010) Mathematical properties relevant to geomagnetic field modeling. In: *Handbook of geomathematics*. https://doi.org/10.1007/978-3-642-01546-5_17
- Sabaka TJ, Olsen N, Tyler RH et al (2015) CM5, a pre-Swarm comprehensive geomagnetic field model derived from over 12 yr of CHAMP, Ørsted, SAC-C and observatory data. *Geophys J Int* 200(3):1596–1626. <https://doi.org/10.1093/gji/ggu493>
- Sabaka TJ, Tyler RH, Olsen N (2016) Extracting ocean-generated tidal magnetic signals from Swarm data through satellite gradiometry. *Geophys Res Lett* 43(7):3237–3245. <https://doi.org/10.1002/2016GL068180>
- Sabaka TJ, Tøffner-Clausen L, Olsen N et al (2018) A comprehensive model of Earth's magnetic field determined from 4 years of Swarm satellite observations. *Earth Planets Space* 70(1):1–26. <https://doi.org/10.1186/s40623-018-0896-3>
- Sabaka TJ, Tøffner-Clausen L, Olsen N et al (2020) CM6: a comprehensive geomagnetic field model derived from both CHAMP and Swarm satellite observations. *Earth Planets Space* 72(1):1–24. <https://doi.org/10.1186/s40623-020-01210-5>
- Šachl L, Velínský J, Fulla J et al (2022) Inversion of the satellite observations of the tidally induced magnetic field in terms of 3-D upper-mantle electrical conductivity: method and synthetic tests. *Geophys J Int* 229(3):2115–2132. <https://doi.org/10.1093/gji/ggac015>
- Sato S (2020) Altitude effects of localized source currents on magnetotelluric responses. *Earth Planets Space* 72:1–8. <https://doi.org/10.1186/s40623-020-01200-7>
- Saur J, Neubauer FM, Glassmeier KH (2010) Induced magnetic fields in solar system bodies. *Space Sci Rev* 152:391–421. <https://doi.org/10.1007/s11214-009-9581-y>
- Saur J, Duling S, Roth L et al (2015) The search for a subsurface ocean in Ganymede with Hubble Space Telescope observations of its auroral ovals. *J Geophys Res Space Phys* 120(3):1715–1737. <https://doi.org/10.1002/2014ja020778>

- Saynisch J, Irrgang C, Thomas M (2018) Estimating ocean tide model uncertainties for electromagnetic inversion studies. *Annales geophysicae*. Copernicus Publications Göttingen, Germany, pp 1009–1014. <https://doi.org/10.5194/angeo-36-1009-2018>
- Saynisch-Wagner J, Baerenzung J, Hornschild A et al (2021) Tide-induced magnetic signals and their errors derived from CHAMP and Swarm satellite magnetometer observations. *Earth Planets Space* 73:1–11. <https://doi.org/10.1186/s40623-021-01557-3>
- Schaeffer N, Jault D (2016) Electrical conductivity of the lowermost mantle explains absorption of core torsional waves at the equator. *Geophys Res Lett* 43(10):4922–4928. <https://doi.org/10.1002/2016gl068301>
- Schmucker U (1985) 4.1.1.4 Equivalent currents: Datasheet from Landolt-Börnstein - Group V Geophysics - Volume 2B: "Subvolume B" in SpringerMaterials https://doi.org/10.1007/10201925_11
- Schmucker U (1999) A spherical harmonic analysis of solar daily variations in the years 1964–1965: response estimates and source fields for global induction-II. *Results. Geophys J Int* 136(2):455–476. <https://doi.org/10.1046/j.1365-246x.1999.00743.x>
- Schmucker U (2018) Electromagnetic induction studies with long-periodic geomagnetic variations in Europe-I. Theory and methods of data analysis. In: 27. Schmucker-Weidelt-Kolloquium für Elektromagnetische Tiefenforschung, Deutsche Geophysikalische Gesellschaft e. V., pp 113–185, URL https://gfzpublic.gfz-potsdam.de/pubman/item/item_3208964
- Schnepf NR, Kuvshinov A, Sabaka T (2015) Can we probe the conductivity of the lithosphere and upper mantle using satellite tidal magnetic signals? *Geophys Res Lett* 42(9):3233–3239. <https://doi.org/10.1002/2015gl063540>
- Schnepf NR, Nair M, Maute A et al (2018) A comparison of model-based ionospheric and ocean tidal magnetic signals with observatory data. *Geophys Res Lett* 45(15):7257–7267. <https://doi.org/10.1029/2018gl078487>
- Schultz A (2010) EMScope: a continental scale magnetotelluric observatory and data discovery resource. *Data Sci J* 8:IGY6–IGY20. https://doi.org/10.2481/dsj.SS_IGY-009
- Schultz A, Egbert G, Kelbert A et al (2018) USArray TA magnetotelluric transfer functions. Tech. rep., <https://doi.org/10.17611/DP/EMTF/USARRAY/TA>
- Schultz A, Bowles-Martinez E, Fry B et al (2020) USMTArray South Magnetotelluric Transfer Functions. Tech. rep., <https://doi.org/10.17611/DP/EMTF/USMTARRAY/SOCAL>
- Schultz A, Pellerin L, Bedrosian P et al (2023) USMTArray South Magnetotelluric Transfer Functions. Tech. rep., <https://doi.org/10.17611/DP/EMTF/USMTARRAY/SOUTH>
- Schuster A (1889) XV. The diurnal variation of terrestrial magnetism. *Philos Trans R Soc Lond (A)* 180:467–518. <https://doi.org/10.1098/rspa.1907.0078>
- Selway K (2014) On the causes of electrical conductivity anomalies in tectonically stable lithosphere. *Surv Geophys* 35:219–257. <https://doi.org/10.1007/s10712-013-9235-1>
- Semenov A, Kuvshinov A (2012) Global 3-D imaging of mantle conductivity based on inversion of observatory C-responses-II. Data analysis and results. *Geophys J Int* 191(3):965–992. <https://doi.org/10.1111/j.1365-246X.2012.05665.x>
- Seufert M, Saur J, Neubauer FM (2011) Multi-frequency electromagnetic sounding of the Galilean moons. *Icarus* 214(2):477–494. <https://doi.org/10.1016/j.icarus.2011.03.017>
- Shimizu H, Utada H, Baba K et al (2010) Three-dimensional imaging of electrical conductivity in the mantle transition zone beneath the North Pacific Ocean by a semi-global induction study. *Phys Earth Planet Inter* 183(1–2):252–269. <https://doi.org/10.1016/j.pepi.2010.01.010>
- Shimizu H, Yoneda A, Baba K et al (2011) Sq effect on the electromagnetic response functions in the period range between 10^4 and 10^5 s. *Geophys J Int* 186(1):193–206. <https://doi.org/10.1111/j.1365-246x.2011.05036.x>
- Shimizu H, Matsushima M, Takahashi F et al (2013) Constraint on the lunar core size from electromagnetic sounding based on magnetic field observations by an orbiting satellite. *Icarus* 222(1):32–43. <https://doi.org/10.1016/j.icarus.2012.10.029>
- Shimizu H, Momoki N, Toh H et al (2021) Electromagnetic induction revealed by MESSENGER's vector magnetic data: the size of Mercury's core. *Icarus* 354(114):112. <https://doi.org/10.1016/j.icarus.2020.114112>
- Singh A, Dehiya R (2023) 3D inversion scheme for high-resolution analysis of continental scale Magnetotelluric data. *Authorea Preprints* <https://doi.org/10.22541/essoar.169111798.83457902/v1>
- Sonett C (1975) Solar-wind induction and lunar conductivity. *Phys Earth Planet Inter* 10(3):313–322. [https://doi.org/10.1016/0031-9201\(75\)90057-6](https://doi.org/10.1016/0031-9201(75)90057-6)
- Srivastava S (1966) Theory of the magnetotelluric method for a spherical conductor. *Geophys J Int* 11(4):373–387. <https://doi.org/10.1111/j.1365-246x.1966.tb03090.x>

- Stammer D, Ray R, Andersen OB et al (2014) Accuracy assessment of global barotropic ocean tide models. *Rev Geophys* 52(3):243–282. <https://doi.org/10.1002/2014rg000450>
- Stolle C, Michaelis I, Xiong C et al (2021) Observing Earth's magnetic environment with the GRACE-FO mission. *Earth Planets Space* 73:1–21. <https://doi.org/10.1186/s40623-021-01364-w>
- Straume EO, Gaina C, Medvedev S et al (2019) GlobSed: updated total sediment thickness in the world's oceans. *Geochem Geophys Geosyst* 20(4):1756–1772. <https://doi.org/10.1029/2018gc008115>
- Strugarek A (2017) Models of star-planet magnetic interaction. Springer International Publishing, Cham, pp 1–23. https://doi.org/10.1007/978-3-319-55333-7_25
- Styp-Rekowski K, Michaelis I, Stolle C et al (2022) Machine learning-based calibration of the GOCE satellite platform magnetometers. *Earth Planets Space* 74(1):1–23. <https://doi.org/10.21203/rs.3.rs-1607576/v1>
- Sun J, Egbert G (2012) A thin-sheet model for global electromagnetic induction. *Geophys J Int* 189(1):343–356. <https://doi.org/10.1111/j.1365-246x.2012.05383.x>
- Sun J, Kelbert A, Egbert GD (2015) Ionospheric current source modeling and global geomagnetic induction using ground geomagnetic observatory data. *J Geophys Res Solid Earth* 120(10):6771–6796. <https://doi.org/10.1002/2015jb012063>
- Tanskanen E (2009) A comprehensive high-throughput analysis of substorms observed by IMAGE magnetometer network: years 1993–2003 examined. *J Geophys Res Space Phys.* <https://doi.org/10.1029/2008ja013682>
- Thiel S, Goleby BR, Pawley MJ et al (2020) AusLAMP 3D MT imaging of an intracontinental deformation zone, Musgrave Province, Central Australia. *Earth Planets Space* 72(1):1–21. <https://doi.org/10.1186/s40623-020-01223-0>
- Thomson AWP, Flower SM (2021) Modernizing a global magnetic partnership. *Eos.* <https://doi.org/10.1029/2021EO156569>
- Toepfer S, Narita Y, Glassmeier KH et al (2021) The Mie representation for Mercury's magnetic field. *Earth Planets Space* 73:1–18. <https://doi.org/10.1186/s40623-021-01386-4>
- Tsyganenko N (2013) Data-based modelling of the Earth's dynamic magnetosphere: a review. *Annales geophysicae.* Copernicus Publications Göttingen, Germany, pp 1745–1772. <https://doi.org/10.5194/angeo-31-1745-2013>
- Tyler RH, Maus S, Luhr H (2003) Satellite observations of magnetic fields due to ocean tidal flow. *Science* 299(5604):239–241. <https://doi.org/10.1126/science.1078074>
- Tyler RH, Boyer TP, Minami T et al (2017) Electrical conductivity of the global ocean. *Earth Planets Space* 69(1):1–10. <https://doi.org/10.1186/s40623-017-0739-7>
- Vance SD, Styczinski M, Bills B et al (2021) Magnetic induction responses of Jupiter's ocean moons including effects from adiabatic convection. *J Geophys Res Planets* 126(2):e2020JE006418. <https://doi.org/10.1029/2020je006418>
- Vanyan L (1980) The electrical conductivity of the Moon. *Geophys Surv* 4(1–2):173–185. <https://doi.org/10.1007/bf01452965>
- Velínský J, Finlay C (2011) Effect of a metallic core on transient geomagnetic induction. *Geochem Geophys Geosyst.* <https://doi.org/10.1029/2011gc003557>
- Velínský J, Knopp O (2021) Lateral variations of electrical conductivity in the lower mantle constrained by Swarm and CryoSat-2 missions. *Earth Planets Space* 73(1):1–12. <https://doi.org/10.1186/s40623-020-01334-8>
- Velínský J, Benešová N, Čížková H (2012) On the detectability of 3-D postperovskite distribution in D'' by electromagnetic induction. *Phys Earth Planet Inter* 202:71–77. <https://doi.org/10.1016/j.pepi.2012.02.012>
- Velínský J, Grayver A, Kuvshinov A et al (2018) On the modelling of M-2 tidal magnetic signatures: effects of physical approximations and numerical resolution. *Earth Planets Space.* <https://doi.org/10.1186/s40623-018-0967-5>
- Velínský J, Sachl L, Martinec Z (2019) The global toroidal magnetic field generated in the Earth's oceans. *Earth Planet Sci Lett* 509:47–54. <https://doi.org/10.1016/j.epsl.2018.12.026>
- Velínský J, Schnepf NR, Nair MC et al (2021) Can seafloor voltage cables be used to study large-scale circulation? An investigation in the Pacific Ocean. *Ocean Sci* 17(1):383–392. <https://doi.org/10.5194/os-17-383-2021>
- Verhoeven O, Thébaud E, Saturnino D et al (2021) Electrical conductivity and temperature of the Earth's mantle inferred from Bayesian inversion of Swarm vector magnetic data. *Phys Earth Planet Inter* 314(106):702. <https://doi.org/10.1016/j.pepi.2021.106702>
- Wang L, Hitchman AP, Ogawa Y et al (2014) A 3-D conductivity model of the Australian continent using observatory and magnetometer array data. *Geophys J Int* 198(2):1143–1158. <https://doi.org/10.1093/gji/ggu188>

- Wang N, Yin C, Gao L et al (2023) 3-D anisotropic modelling of geomagnetic depth sounding based on unstructured edge-based finite-element method. *Geophys J Int* 235(1):178–199. <https://doi.org/10.1093/gji/ggad224>
- Wardinski I, Langlais B, Thébault E (2019) Correlated time-varying magnetic fields and the core size of Mercury. *J Geophys Res Planets* 124(8):2178–2197. <https://doi.org/10.1029/2018je005835>
- Weber T, Moore K, Connerney J et al (2022) Updated spherical harmonic magnetic field moments of Ganymede from the Juno flyby. *Geophys Res Lett* 49(23):e2022GL098633. <https://doi.org/10.1029/2022gl098633>
- Weidelt P (1972) The inverse problem of geomagnetic induction. *Z Geophys* 38:257–289. <https://doi.org/10.1093/gji/35.1.379>
- Weidelt P, Chave AD (2012) The magnetotelluric response function. Cambridge University Press, Cambridge, pp 122–164. <https://doi.org/10.1017/CBO9781139020138.006>
- Weiss BP, Biersteker JB, Colicci V et al (2021) Searching for subsurface oceans on the moons of Uranus using magnetic induction. *Geophys Res Lett* 48(19):e2021GL094758. <https://doi.org/10.1002/essoar.10507412.1>
- Yamazaki Y (2022) Solar and lunar daily geomagnetic variations and their equivalent current systems observed by Swarm. *Earth Planets Space* 74(1):99. <https://doi.org/10.1186/s40623-022-01656-9>
- Yamazaki Y, Maute A (2017) Sq and EEJ-A review on the daily variation of the geomagnetic field caused by ionospheric dynamo currents. *Space Sci Rev* 206(1–4):299–405. https://doi.org/10.1007/978-94-024-1225-3_12
- Yang B, Egbert GD, Zhang H et al (2021) Electrical resistivity imaging of continental United States from three-dimensional inversion of EarthScope USArray magnetotelluric data. *Earth Planet Sci Lett* 576(117):244. <https://doi.org/10.1016/j.epsl.2021.117244>
- Yao H, Ren Z, Tang J et al (2022) A multi-resolution finite-element approach for global electromagnetic induction modeling with application to southeast China coastal geomagnetic observatory studies. *J Geophys Res Solid Earth* 127(8):e2022JB024659. <https://doi.org/10.1029/2022jb024659>
- Yao H, Ren Z, Pan K et al (2023) A global mantle conductivity model derived from 8 years of Swarm satellite magnetic data. *Earth Planet Phys* 7(1):49–56. <https://doi.org/10.26464/epp2023011>
- Yao H, Ren Z, Tang J et al (2023) Trans-dimensional Bayesian joint inversion of magnetotelluric and geomagnetic depth sounding responses to constrain mantle electrical discontinuities. *Geophys J Int* 233(3):1821–1846. <https://doi.org/10.1093/gji/ggad029>
- Yoshino T (2021) Electrical properties of rocks. Encyclopedia of solid earth geophysics. Springer, Berlin, pp 339–344. https://doi.org/10.1007/978-3-030-58631-7_45
- Yoshino T, Katsura T (2013) Electrical conductivity of mantle minerals: role of water in conductivity anomalies. *Annu Rev Earth Planet Sci* 41:605–628. <https://doi.org/10.1146/annurev-earth-050212-124022>
- Yuan Y, Uyeshima M, Huang Q et al (2020) Continental-scale deep electrical resistivity structure beneath China. *Tectonophysics* 790(228):559. <https://doi.org/10.1016/j.tecto.2020.228559>
- Zenhäusern G, Kuvshinov A, Guzavina M et al (2021) Towards probing Earth's upper mantle with daily magnetic field variations: exploring a physics-based parametrization of the source. *Earth Planets Space* 73(1):1–16. <https://doi.org/10.1186/s40623-021-01455-8>
- Zhang H, Egbert G, Chave A et al (2019) Constraints on the resistivity of the oceanic lithosphere and asthenosphere from seafloor ocean tidal electromagnetic measurements. *Geophys J Int* 219(1):464–478. <https://doi.org/10.1093/gji/ggz315>
- Zhang H, Egbert GD, Huang Q (2022) A relatively dry mantle transition zone revealed by geomagnetic diurnal variations. *Sci Adv* 8(31):eabo3293. <https://doi.org/10.1126/sciadv.abo3293>
- Zhang H, Egbert G, Huang Q (2023) Constraints on MTZ water content from joint inversion of diurnal variations and magnetospheric signals. *Geophys Res Lett* 50(10):e2023GL102765. <https://doi.org/10.1029/2023gl102765>
- Zhang X, Lomas A, Zhou M et al (2023) 3D Bayesian Variational Full Waveform Inversion. *Geophys J Int*. <https://doi.org/10.1093/gji/ggad057>
- Zhang Y, Yang Y (2022) Three-dimensional inversion resolution in detecting stagnant slabs using a dense geomagnetic depth sounding method. *Phys Earth Planet Inter* 333(106):955. <https://doi.org/10.1016/j.pepi.2022.106955>
- Zhang Y, Weng A, Li S et al (2020) Electrical conductivity in the mantle transition zone beneath Eastern China derived from L1-Norm C-responses. *Geophys J Int* 221(2):1110–1124. <https://doi.org/10.1093/gji/ggaa059>
- Zhang Y, Yang Y, Wang X et al (2021) C-responses estimation of geomagnetic depth sounding using regularization method and its application in Northeast China. *J Appl Geophys* 195(104):475. <https://doi.org/10.1016/j.jappgeo.2021.104475>

- Zhao X, Curtis A, Zhang X (2022) Bayesian seismic tomography using normalizing flows. *Geophys J Int* 228(1):213–239. <https://doi.org/10.1093/gji/ggab298>
- Zomerdiijk-Russell S, Masters A, Heyner D (2021) Variability of the interplanetary magnetic field as a driver of electromagnetic induction in Mercury's interior. *J Geophys Res Space Phys* 126(10):e2021JA029,664. <https://doi.org/10.1029/2021ja029664>
- Zomerdiijk-Russell S, Masters A, Korth H et al (2023) Modeling the time-dependent magnetic fields that BepiColombo will use to probe down into Mercury's mantle. *Geophys Res Lett* 50(2):e2022GL101,607. <https://doi.org/10.1029/2022GL101607>

Publisher's Note Springer Nature remains neutral with regard to jurisdictional claims in published maps and institutional affiliations.